

Soliton nanoantennas in two-dimensional arrays of quantum dots

G. Gligorić, A. Maluckov, and Lj. Hadžievski

P* group, Vinča Institute of Nuclear Sciences, University of Belgrade, P. O. B. 522,11001 Belgrade, Serbia

G. Ya. Slepyan, and B. A. Malomed

Department of Physical Electronics, School of Electrical Engineering, Faculty of Engineering, Tel Aviv University, Tel Aviv 69978, Israel

E-mail: sandram@vin.bg.ac.rs

Abstract. We consider two-dimensional (2D) arrays of self-organized semiconductor quantum dots (QDs) strongly interacting with electromagnetic field in the regime of Rabi oscillations. The QD array built of two-level states is modelled by two coupled systems of discrete nonlinear Schrödinger equations. Localized modes in the form of single-peaked fundamental and vortical stationary Rabi solitons and self-trapped breathers have been found. The results for the stability, mobility and radiative properties of the Rabi modes suggest a concept of a self-assembled 2D *soliton-based nano-antenna*, which should be stable against imperfections. In particular, we discuss the implementation of such a nano-antenna in the form of surface plasmon solitons in graphene, and illustrate possibilities to control their operation by means of optical tools.

PACS numbers: 05.45.Yv; 68.65.Hb; 78.67.Ch; 73.21.-b

P* group, Vinča Institute of Nuclear Sciences, University of Belgrade, P. O. B. 522,11001 Belgrade, Serbia

Department of Physical Electronics, School of Electrical Engineering, Faculty of Engineering, Tel Aviv University, Tel Aviv 69978, Israel

E-mail: sandram@vin.bg.ac.rs

Keywords: two-dimensional dynamical lattices, Rabi solitons, discrete solitons, quantum dots, nano-antenna

1. Introduction

Experimental and theoretical studies of solitons in nonlinear lattices are the field of intensive activity in several branches of physics. Its large part is focused on nonlinear optics [1] and matter waves (i.e., Bose-Einstein condensates, BEC). The latter may be treated in the mean-field approximation [2], or in terms of the quantum Bose-Hubbard

model [3, 4] (see book [5] for a systematic summary). In these contexts, the discrete nonlinear Schrödinger (DNLS) equation, and systems of the coupled DNLS equations, are ubiquitous dynamical models for the description of nonlinear lattices [6]. In the framework of these studies, the existence, stability, and dynamics (including mobility) of discrete self-trapped modes (discrete solitons) is a topic which has drawn a great deal of interest.

In multi-component systems, couplings between components may be linear, nonlinear, or both linear and nonlinear [6]. In the context of optics, systems of linearly coupled DNLS equations are relevant to various applications. In particular, the linear coupling between two polarization modes in each core of a waveguide array may be induced by a twist of the core (for linear polarizations), or by the birefringence (for circular polarizations). On the other hand, in the BEC the linear coupling may be imposed by an external microwave or radio-frequency field, which can drive Rabi oscillations [7, 8] or Josephson oscillations [9, 10] between two boson populations. In terms of the dynamical analysis, an essential issue is the possibility of the spontaneous symmetry breaking in linearly coupled discrete systems [11].

The progress in the fabrication of nano-scale electric circuits [12], lasers [13], waveguides and antennas, for microwave, tera-Hertz and optical frequency ranges, is another strong incentive stimulating studies of nonlinear lattices. Particularly significant nano-dimensional elements are self-organized quantum-dots (QDs) [14] embedded into semiconductor dielectric host media. The possibility of strong interactions of QDs with optical fields gives rise to Rabi oscillations (RO) between electron-hole populations of ground and excited states. The basic RO model amounts to a two-level atom strongly coupled to an external electromagnetic field (the Jaynes - Cummings model) [15]. For more complex structures, such as large molecules [16] or QDs, this model has been modified to account for additional factors: anisotropy [16], local-field corrections [17]-[20], broken inversion symmetry [21], etc. In these settings, crucially significant are collective coherent effects, stipulated by the inter-dot coupling inside the QD array. Oscillations of the QD population between levels in an isolated two-level system may be considered as energy exchange between the system and the ambient electromagnetic field. On the other hand, particle transfer (e.g., inter-dot electron, or electron-hole tunnelling) leads to the exchange of the quasi-momentum between charge carriers and photons. These mechanisms govern the spatiotemporal RO dynamics in the QD chains, in the form of the propagation of travelling RO waves and wave packets (*Rabi waves*) [22]-[24].

In the QDs arrays the transport can also be realized by tunnelling via the inter-dot dipole-dipole coupling, such as Förster interactions [14], and by the radiation-field transfer. In Ref. [23], the tunnelling was assumed to be a dominant mechanism of the inter-dot coupling. In that case, a significant role is played by local-field effects in the QDs, even in the weak-coupling regime [17, 18]. The local-field effects, enhanced by the strong light-QD coupling, modify the conventional RO dynamics [22]-[24]. As a result, specific nonlinear terms appear in equations of electron-hole oscillations inside the QDs,

braking the superposition principle for the single-particle wave function. The role of local fields in the formation of excitonic RO in self-assembling QDs was experimentally studied in Refs. [25, 26].

The nonlinearity affects the Rabi-wave propagation too. As was shown in Ref. [27], solitons and self-trapped breathers in the one-dimensional (1D) QD chains can be created with the help of the nonlinearity. The model developed in Ref. [27] explores the dynamics of the probability amplitudes of the ground and excited states of QDs, with included nonlinear cross-phase-modulation terms and linear coupling between the two states. The phase shift between constants of the inter-site hopping is a new property introduced geometrically in that 1D setting.

Recently, theoretical and experimental studies of nano-antennas have been in a focus of work performed by many groups. The antenna is defined as a device which transforms the near field into the far field, or vice versa (transmitting and receiving antennas, respectively). Transmitting devices produce the spherical wave in a remote spatial area, with electric field

$$\mathbf{E}_{\text{Rad}} = \frac{\mathbf{e}_\theta}{4\pi\epsilon_0} \frac{\omega^2}{c^2} \mathbf{E}_0 \frac{e^{-i\omega(t-R/c)}}{R} F(\theta, \varphi) + c.c., \quad (1)$$

where R, θ, φ are the spherical coordinates, with the origin set at the center of the antenna, $F(\theta, \varphi)$ is a normalized angular radiation pattern, ϵ_0 is the vacuum permittivity, c is the free-space light velocity, \mathbf{e}_θ is the unit vector along the local direction of coordinate θ , with \mathbf{E}_0 and ω being the amplitude and frequency of the electric field, respectively. The purport of using the antennas is their ability to provide an interface between local information processing, which uses electrical signals, and the free-space wireless transmission of data encoded in various parameters of the electromagnetic waves, such as the amplitude, phase and frequency.

Directional antenna properties (the dependence of the emitted field on both the azimuthal and polar angles) are characterized by the radiation pattern. It is determined by the near-field distribution produced by the signal source placed inside the antenna. It depends on the frequency, antenna configuration and geometric parameters. An important species of the device is represented by phased antenna arrays, i.e., systems of a large number of identical emitters with a phase shift between adjacent ones [28]. The progress in the fabrication of nano-antennas, see Refs. [29]–[31] for review, manifests the general trend of implementing radio-communication principles in the optical-frequency range. In particular, it stimulates bridging the realms of macroscopic antennas and nano-antennas, using new materials with specific electronic properties. In this context, it is relevant to mention carbon nanotubes and nanotube arrays [32]–[35], plasmonic noble-metal wires [36, 37], graphene nanoribbons [38], semiconductor QDs [39, 41], etc. These types of nano-antennas have been offered as promising elements for industrial design and commercial manufacturing. However, many limitations for their use are stipulated by difficulties of their operational control – for instance, rotation of the radiation pattern by an electric or optical drive. This difficulty, along with the growing interest to the field, motivate the search of new physical principles for fabrication and tuning of nano-

antennas. A promising possibility for that is suggested by using strong nonlinearities in nanostructures (in particular, remarkable nonlinear properties of graphene [42, 43]).

In this work, we propose a previously unexplored principle for the realization of nano-antenna arrays in the form of self-trapping *discrete solitons* in 2D nonlinear lattices built of semiconductor QDs. In this context, dynamically stable soliton structures (fundamental discrete solitons, vortex solitons, and breathers) may provide promising mechanisms of controllable creation of the antennas with various geometric shapes. The model for the 2D array of QDs can be developed from its 1D counterpart which was elaborated in Ref. [27]; obviously, the transition from 1D to the 2D geometry is a crucially important step for modelling antennas which emit in the plane of the semiconductor structure. We demonstrate that different types of the global drive, *viz.*, plane and cylindrical waves, can excite Rabi oscillations and waves in the system. Using known numerical techniques developed for the study of discrete solitons [6], we construct basic localized modes of the corresponding 2D DNLS equations and test their stability and mobility. In addition, we demonstrate how discrete Rabi solitons induce the dielectric polarization, and thus build the near-field of the soliton-based nano-antenna. On the contrary to other radiation zones, the near field keeps itself in a quantum state, which helps to establish the correlation of quantum effects and field transformation between different spatial zones. We also present the far-field structure produced by the given near field, which takes into account the quantum nature of the underlying Rabi oscillator.

The paper is organized as follows. In Sec. II, we introduce the model for the 2D QD array interacting with the driving electromagnetic field. As mentioned above, the plane- and cylindrical-wave drives are considered. The nonlinearity is induced as the local-field effect. The model is analyzed numerically, with the purpose to reveal the RO dynamics in the QD arrays. In Sec. III, necessary technical ingredients are introduced, including the dispersion relation for the linearized system, and general expressions for radiation properties generated by solitons in the 2D QD array. In Sec. IV, results are presented in detail, and the relation of the present model to 2D nano-antenna arrays is proposed. The important issue of maintaining the coherence of emitters building the soliton nano-antenna is considered in Sec. IV too, and possibilities for operational control of the device by means of optical tools are outlined. The paper is summarized in Sec. V.

2. Two-dimensional model equations

2.1. The plane-wave drive

We consider finite 2D rectangular $N_1 \times N_2$ array of identical QDs with the square unit cell of size $a \times a$ (a is the inter-dot distance). The position of QDs is defined by a pair of discrete indices, $p = -N_1/2, \dots, N_1/2$ and $q = -N_2/2, \dots, N_2/2$. The array is exposed

to the classical travelling optical wave of in the xy - plane with electric field

$$\mathbf{E}(x, y, t) = \text{Re} \{ \mathbf{E}_0 \exp [ik (x \cos \theta_0 + y \sin \theta_0) - i\omega t] \}, \quad (2)$$

where $k = k(\omega)$ is the wavenumber and θ_0 is the propagation angle (see Fig. 1 (a)). The driving field may represent different types of the electromagnetic modes, the first one being a plane wave with a nonzero E_z component. Another example is a surface plasmon guided by the plane boundary between the noble metal and transparent medium [14], on which the QD array is installed. The latter example comes with the frequency dispersion of a plasma medium, which manifests itself in a nonlinear dependence $k = k(\omega)$. We take QDs as identical two-level dissipationless systems with the transition energy, $\hbar\omega_0$, corresponding to the transition between excited and ground-state electron orbitals, $|a_{p,q}\rangle$ and $|b_{p,q}\rangle$. The transition dipolar moment is $\mu = \mathbf{e}_z\mu$, and only intraband transitions are taken into account [23]. Each QD is coupled by the electron tunnelling to four nearest neighbors in the 2D array.

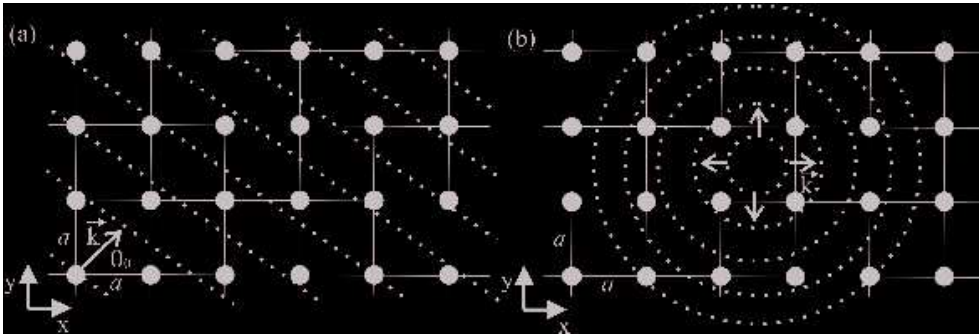


Figure 1. Schematically presented plane wave (a) and cylindrical wave (b) drive of 2D QD array placed in the (x, y) plane. Dotted curves display wave fronts in both cases, \vec{k} is the wave-vector, θ_0 is the propagation angle and a is the inter-dot distance.

It is adopted that the light interaction within the QD chain takes place in the resonant regime, i.e., the frequency detuning is small in comparison to both the light and quantum-transition frequencies. Following the rotation-wave-approximation [15], we omit rapidly oscillating terms in the equations of motion. These natural assumptions follows the Rabi-waves model formulated in Ref. [23].

The raising, lowering, and population operators of the QD by denoted as $\hat{\sigma}_{p,q}^+ = |a_{p,q}\rangle\langle b_{p,q}|$, $\hat{\sigma}_{p,q}^- = |b_{p,q}\rangle\langle a_{p,q}|$, and $\hat{\sigma}_{zp,q} = |a_{p,q}\rangle\langle a_{p,q}| - |b_{p,q}\rangle\langle b_{p,q}|$, respectively. The total Hamiltonian is

$$\hat{H} = \hat{H}_d + \hat{H}_{df} + \hat{H}_T + \Delta\hat{H}, \quad (3)$$

where the term

$$\hat{H}_d = \frac{\hbar\omega_0}{2} \sum_{p,q} \hat{\sigma}_{zp,q} \quad (4)$$

describes the free electron motion, while the one

$$\hat{H}_{df} = -(\mu\mathbf{E}_0) \sum_{p,q} \hat{\sigma}_{p,q}^+ \exp(i(p\phi_1 + q\phi_2)) + \text{H.c.} \quad (5)$$

(H.c. stands for Hermitian-conjugate operator) accounts for the interaction of QD array with the electromagnetic field in the dipole approximation without tunnelling. Here, phases

$$\phi_1 = (ka/2) \cos(\theta), \phi_2 = (ka/2) \sin(\theta). \quad (6)$$

represent the field delay per lattice period due to the finite propagation speed. The limit of $\phi_{1,2} \rightarrow 0$ corresponds to the dense lattice, with $ka \gg 1$.

The third term in Eq. (3) corresponds to the inter-dot coupling through the tunnelling. To interpret, it we introduce tunnelling coupling factors $\xi_{p,q}^{(a,b)}$ which are step functions of the discrete spatial coordinates, p and q :

$$\xi_{p,q}^{(a,b)} = \begin{cases} \xi^{(a,b)}, & p, q = -(N_{1,2}/2), \dots - 1, 0, 1, \dots, N_{1,2}/2, \\ 0, & \text{in all other cases.} \end{cases} \quad (7)$$

The Hamiltonian of the tunnelling interaction is, in the tight-binding approximation,

$$\begin{aligned} \hat{H}_T = & -\hbar \sum_{p,q} (\xi_{p+1,q}^{(a)} |a_{p,q}\rangle \langle a_{p+1,q}| + \xi_{p,q}^{(a)} |a_{p,q}\rangle \langle a_{p-1,q}| + \xi_{p,q+1}^{(a)} |a_{p,q}\rangle \langle a_{p,q+1}| + \xi_{p,q}^{(a)} |a_{p,q}\rangle \langle a_{p,q-1}|) \\ & -\hbar \sum_{p,q} (\xi_{p+1,q}^{(b)} |b_{p,q}\rangle \langle b_{p+1,q}| + \xi_{p,q}^{(b)} |b_{p,q}\rangle \langle b_{p-1,q}| + \xi_{p,q+1}^{(b)} |b_{p,q}\rangle \langle b_{p,q+1}| + \xi_{p,q}^{(b)} |b_{p,q}\rangle \langle b_{p,q-1}|). \end{aligned} \quad (8)$$

Coefficients $\xi^{(a,b)}$ in Eq. (8) are accounted for the tunnelling coupling between adjacent QDs in the excited and ground states, respectively. They are defined as scalars due to the isotropy of individual QDs and the array. The step-like structure in Eq. (7) corresponds to the operator notation for the tunnelling in the finite-size array: the number of the adjacent QDs coupled by the tunnelling reduces up to three for sites at *edges* of the array, and to two at *corners*.

The last term in Hamiltonian (3) represents the local-field effects, in the Hartree-Fock-Bogoliubov approximation [17], [27]:

$$\Delta \hat{H} = \frac{4\pi}{V} N_{\alpha,\beta} \mu_{\alpha} \mu_{\beta} \sum_{p,q} (\hat{\sigma}_{p,q}^{-} \langle \hat{\sigma}_{p,q}^{+} \rangle + \hat{\sigma}_{p,q}^{+} \langle \hat{\sigma}_{p,q}^{-} \rangle), \quad (9)$$

where $\mu_{\alpha,\beta}$ and $N_{\alpha,\beta}$ are components of the dipolar-moment vector and depolarization tensor of the single QD, V is the volume of the single QD, and angle brackets denote averaging of the corresponding operator with respect to the given quantum state. The summations over doubly repeated indices have been omitted in accordance with the usual convention. The depolarization tensor depends both on the QD configuration and quantum properties of electron-hole pairs, given by

$$N_{\alpha,\beta} = \frac{V}{4\pi} \int_V \int_V |\xi(\mathbf{r})|^2 |\xi(\mathbf{r}')|^2 G_{\alpha,\beta}(\mathbf{r} - \mathbf{r}') d^3\mathbf{r} d^3\mathbf{r}', \quad (10)$$

where $\xi(\mathbf{r})$ is the envelope of the wave-function of electron-hole pair, and $G_{\alpha,\beta}(\mathbf{r} - \mathbf{r}')$ is the Green's tensor of the Maxwell's equations in the quasi-static limit [14]. The present formulation may be applied to 1D and 2D setting alike [24]. Using the Hartree-Fock-Bogoliubov approximation, local-field effects for the single QD, were investigated

in the strong coupling regime in Refs. [17], and [27], and thereafter demonstrated experimentally [44].

The temporal evolution of single-particle excitations is governed by the Schrödinger equation,

$$i\hbar \frac{\partial |\Psi\rangle}{\partial t} = \hat{H} |\Psi\rangle. \quad (11)$$

The unknown wave function is taken in the form of a coherent superposition,

$$|\Psi\rangle = \sum_{p,q} (\Psi_{p,q}(t) e^{(i/2)(p\phi_1+q\phi_2-\omega t)} |a_{p,q}\rangle + \Phi_{p,q}(t) e^{-(i/2)(p\phi_1+q\phi_2-\omega t)} |b_{p,q}\rangle), \quad (12)$$

where $\Psi_{p,q}(t)$, $\Phi_{p,q}(t)$ are probability amplitudes to be found. Projection of the Schrödinger equation onto the chosen basis leads to the following system of coupled nonlinear evolution equations for the probability amplitudes:

$$\begin{aligned} \frac{\partial \Psi_{p,q}}{\partial t} &= iF\Psi_{p,q} \\ &+ i \left(\xi_{p,q}^{(a)} \Psi_{p-1,q} e^{-i\varphi_1} + \xi_{p+1,q}^{(a)} \Psi_{p+1,q} e^{i\varphi_1} + \xi_{p,q}^{(a)} \Psi_{p,q-1} e^{-i\varphi_2} + \xi_{p,q+1}^{(a)} \Psi_{p,q+1} e^{i\varphi_2} \right) \\ &- ig\Phi_{p,q} - i\Delta\omega |\Phi_{p,q}|^2 \Psi_{p,q}, \\ \frac{\partial \Phi_{p,q}}{\partial t} &= -iF\Phi_{p,q} \\ &+ i \left(\xi_{p,q}^{(b)} \Phi_{p-1,q} e^{i\varphi_1} + \xi_{p+1,q}^{(b)} \Phi_{p+1,q} e^{-i\varphi_1} + \xi_{p,q}^{(b)} \Phi_{p,q-1} e^{i\varphi_2} + \xi_{p,q+1}^{(b)} \Phi_{p,q+1} e^{-i\varphi_2} \right) \\ &- ig\Psi_{p,q} - i\Delta\omega |\Psi_{p,q}|^2 \Phi_{p,q}, \end{aligned} \quad (13)$$

where F is the detuning parameter [27], $g \equiv -\mu\mathbf{E}_0/(2\hbar)$ is QD-field coupling factor, and $\Delta\omega \equiv 4\pi\mu_\alpha\mu_\beta N_{\alpha,\beta}/(\hbar V)$ is the depolarization shift. The normalization condition for system (13) is

$$\sum_{p=-N_1/2}^{N_1/2} \sum_{q=-N_2/2}^{N_2/2} (|\Psi_{p,q}|^2 + |\Phi_{p,q}|^2) = 1. \quad (14)$$

The observable value of the energy is given by

$$\begin{aligned} \varepsilon \equiv \langle \hat{H} \rangle &= \frac{1}{2} \sum_{p=-N_1/2}^{N_1/2} \sum_{q=-N_2/2}^{N_2/2} \left[-F(|\Psi_{p,q}|^2 - |\Phi_{p,q}|^2) \right. \\ &- \Phi_{p,q}^* \left(\xi_{p,q}^{(b)} \Phi_{p-1,q} e^{i\varphi_1} + \xi_{p+1,q}^{(b)} \Phi_{p+1,q} e^{-i\varphi_1} + \xi_{p,q}^{(b)} \Phi_{p,q-1} e^{i\varphi_2} + \xi_{p,q+1}^{(b)} \Phi_{p,q+1} e^{-i\varphi_2} \right) \\ &- \Psi_{p,q}^* \left(\xi_{p,q}^{(a)} \Psi_{p-1,q} e^{-i\varphi_1} + \xi_{p+1,q}^{(a)} \Psi_{p+1,q} e^{i\varphi_1} + \xi_{p,q}^{(a)} \Psi_{p,q-1} e^{-i\varphi_2} + \xi_{p,q+1}^{(a)} \Psi_{p,q+1} e^{i\varphi_2} \right) \\ &\left. + g\Psi_{p,q}^* \Phi_{p,q} + \frac{1}{2}\Delta\omega |\Psi_{p,q}|^2 |\Phi_{p,q}|^2 + \text{c.c.} \right]. \end{aligned} \quad (15)$$

The analysis of the Rabi solitons in the 2D QD lattices is developed below on the basis of Eq. (13).

In the simplest case, one may assume the inter-site coupling coefficients for the ground and excited states to be equal, $\xi^{(a)} = \xi^{(b)} = \xi$. Next, we set, by means of an obvious rescaling, $g = -1$ and $\text{sign}(\Delta\omega) = -1$. These signs imply the attractive onsite

linear interaction between fields $\Psi_{p,q}$ and $\Phi_{p,q}$, and the self-focusing sign of the XPM (cross-phase-modulation, i.e., the cubic interaction between the different components) onsite nonlinearity. Actually, if g is originally positive, it can be made negative by substitution $\Phi_{p,q} = -\tilde{\Phi}_{p,q}$. And if $\Delta\omega$ is originally positive, it may be made negative by means of the usual staggering substitution [6]. Thus, in Eqs. (13) there remain three independent parameters which can be combined into the frequency detuning, F , and the complex lattice coupling, $\xi \exp(i\phi_{1,2})$. We here restrict $\phi_{1,2}$ to the basic interval, $0 \leq \phi_{1,2} \leq \pi/2$, therefore both positive and negative values of F should be considered.

2.2. The cylindrical-wave drive

The spatial structure of Rabi waves is tunable by selecting the corresponding driving field. Of particular interest is cylindrical drive, defined as

$$\mathbf{E}(\mathbf{r}, t) = \mathbf{e}_z \text{Re} \left\{ \mathbf{E}_0 H_0^{(1)}(k|\mathbf{r} - \mathbf{r}_0|) \exp(-i\omega t) \right\}, \quad (16)$$

where $H_0^{(1)}(x)$ is the Hankel function of the zero order and the first type. Such field may be excited by the infinitely thin and infinitely long current wire placed at point \mathbf{r}_0 normally to the array's plane (see Fig. 1 (b)). The current may be produced, for example, by a semiconductor quantum wire excited by the exciton-polariton [45]. The current point \mathbf{r}_0 is placed at the center of the cell consisting of dots with the indices $(p = 0, q = 0)$, $(p = -1, q = -1)$, $(p = 0, q = -1)$ and $(p = -1, q = 0)$. The general statement of the problem is similar to the plane-wave case, the difference being only in the form of the H_{df} component of Hamiltonian (1), which is, now,

$$\hat{H}_{df} = -\mu \mathbf{e}_z E_0 \sum_{p,q} \hat{\sigma}_{p,q}^+ S_{p,q} + H.c., \quad (17)$$

where

$$S_{pq} \equiv \frac{H_0^{(1)} \left(ka \sqrt{(p+1/2)^2 + (q+1/2)^2} \right)}{H_0^{(1)}(ka/\sqrt{2})}. \quad (18)$$

The corresponding equations of motion are

$$\begin{aligned} \frac{\partial \Psi_{p,q}}{\partial t} &= iF \Psi_{p,q} \\ &+ i \left[\xi_{p,q}^{(a)} \Psi_{p-1,q} \varsigma_{pq}^{p-1,q} + \xi_{p+1,q}^{(a)} \Psi_{p+1,q} \varsigma_{pq}^{p+1,q} + \xi_{p,q}^{(a)} \Psi_{p,q-1} \varsigma_{pq}^{p,q-1} + \xi_{p,q+1}^{(a)} \Psi_{p,q+1} \varsigma_{pq}^{p,q+1} \right] \\ &- ig |S_{pq}| \Phi_{p,q} - i\Delta\omega |S_{pq}| |\Phi_{p,q}|^2 \Psi_{p,q}, \\ \frac{\partial \Phi_{p,q}}{\partial t} &= -iF \Phi_{p,q} \\ &+ i \left[\xi_{p,q}^{(b)} \Phi_{p-1,q} \varsigma_{pq}^{*p-1,q} + \xi_{p+1,q}^{(b)} \Phi_{p+1,q} \varsigma_{pq}^{*p+1,q} + \xi_{p,q}^{(b)} \Phi_{p,q-1} \varsigma_{pq}^{*p,q-1} + \xi_{p,q+1}^{(b)} \Phi_{p,q+1} \varsigma_{pq}^{*p,q+1} \right] \\ &- ig |S_{pq}| \Psi_{p,q} - i\Delta\omega |S_{pq}| |\Psi_{p,q}|^2 \Phi_{p,q}, \end{aligned} \quad (19)$$

$$\varsigma_{pq}^{mn} \equiv \sqrt{\frac{S_{mn}}{S_{pq}}}, \quad (20)$$

supplemented by the normalization condition:

$$\sum_{p=-N_1/2}^{N_1/2} \sum_{q=-N_2/2}^{N_2/2} (|\Psi_{p,q}|^2 + |\Phi_{p,q}|^2) |S_{pq}| = 1. \quad (21)$$

Actually, Eq. (19) describes other types of driving field too. Namely, substitution $k \rightarrow i k$ (for real k) transforms the Hankel function into the correspondent Macdonald function $K_0(x)$, which represents driving the Rabi wave by surface plasmons guided by a noble-metal wire [14], or carbon nanotube [46].

3. 2D Rabi solutions

3.1. Dispersion relations

In the limit of $\Delta\omega = 0$, Eq. (13) without the local-field terms reduces to the 2D generalization of the Rabi-wave model considered in Refs. [22, 24]. In this case, the dispersion relation can be derived by looking for solutions as

$$\{\Psi_{p,q}, \Phi_{p,q}\} = \{A, B\} \exp(i(\kappa_x p + \kappa_y q)) \exp(-i\Omega t), \quad (22)$$

where $\kappa_{x,y}$ are wavenumbers, A, B are unknown wave amplitudes, and Ω is an unknown frequency.

A straightforward analysis yields two branches of the dispersion relation,

$$\begin{aligned} \Omega_{1,2}(\kappa_x, \kappa_y) = & -2\xi [\cos(\kappa_x) \cos(\phi_1) + \cos(\kappa_y) \cos(\phi_2)] \\ & \pm \sqrt{g^2 + \{F - 2\xi [\sin(\kappa_x) \sin(\phi_1) + \sin(\kappa_y) \sin(\phi_2)]\}^2}, \end{aligned} \quad (23)$$

examples of which are shown in Fig. 2 for $g = -1$ and $\xi = 1$.

In the limit of $\phi_1 = \phi_2 = \phi = 0$, Eq. (23) goes over into the known dispersion relation for the usual system of linearly coupled 2D DNLS equations, cf. Ref. [6]. It features two similar branches shifted by a constant, $\Delta\Omega = 2\sqrt{g^2 + F^2}$, and corresponds to the Rabi waves. In the case of $\phi_1, \phi_2 \neq 0$, shift $\Delta\Omega$ is no longer constant, as it depends on wavenumbers κ_x and κ_y .

Note that

$$\Omega(\kappa_x, \kappa_y, \phi_1, \phi_2) = \Omega(-\kappa_x, -\kappa_y, -\phi_1, -\phi_2), \quad (24)$$

but

$$\Omega(\kappa_x, \kappa_y, \phi_1, \phi_2) \neq \Omega(-\kappa_x, -\kappa_y, \phi_1, \phi_2). \quad (25)$$

Equation (24) shows that the inversion of the propagation direction of the driving field inverts the direction of the Rabi-wave propagation. This is according to the non-reciprocity of Rabi-waves in 1D chains, noted in Ref. [39].

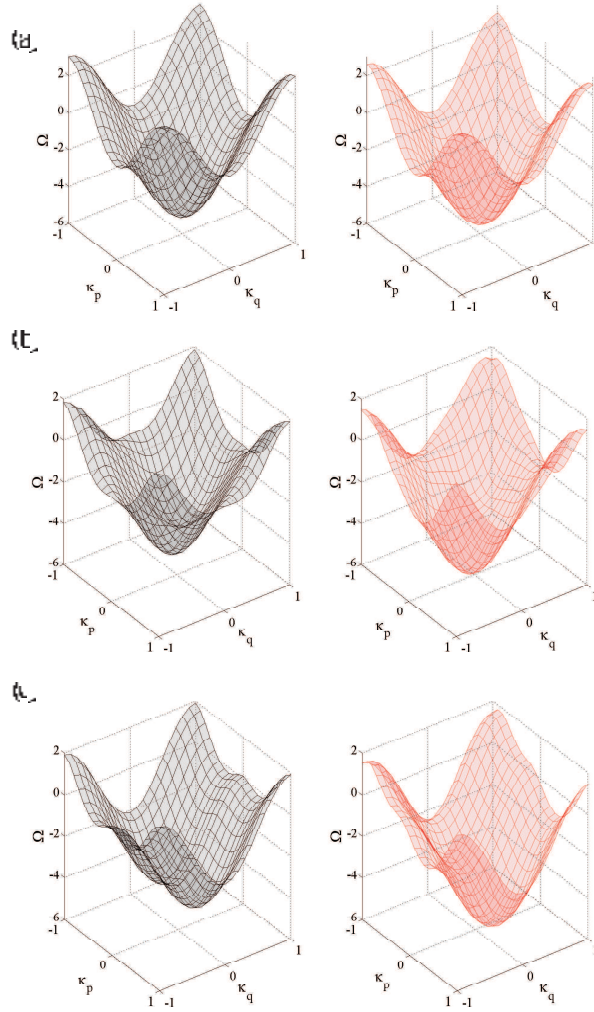


Figure 2. (Color online) Dispersion curves $\Omega = \Omega_2(\kappa_p, \kappa_q)$ for the linearized system with the plane-wave excitation: $F = 0$ (black surfaces), $F = 1$ (red surfaces), and $\phi_1 = \phi_2 = 0$ (a), $\phi_1 = \phi_2 = \pi/4$ (b), $\phi_1 = 0, \phi_2 = \sqrt{2}\pi/4$ (c). Other coefficients are $\xi = 1$ and $g = -1$. Discrete solitons are expected to exist in the semi-infinite gap.

3.2. Constructing Rabi solitons and their radiation patterns

Equations (13) may give rise to stationary discrete 2D fundamental solitons and vortices, looking for localized solutions as

$$\Psi_{p,q} = e^{-i\Omega t} A_{p,q}, \quad \Phi_{p,q} = e^{-i\Omega t} B_{p,q}, \quad (26)$$

where Ω is the corresponding carrier frequency, and $A_{p,q}, B_{p,q}$ are localized complex lattice fields vanishing at infinity (in terms of the numerical solutions, they vanish at boundaries of the computation domain). Stationary soliton solutions of Eqs. (13) were numerically obtained by adopting the nonlinear equation solver based on the Powell method while direct dynamical simulations were based on the Runge-Kutta procedure of the sixth order, [47], [48]. The numerical solution was constructed for a finite lattice

of size 21×21 (unless stated otherwise), with periodic boundary conditions. We have checked that a larger lattice produces the same results.

The emitted field is described by the field operator in the Heisenberg representation [15],

$$\hat{\mathbf{E}}(\mathbf{r}, t) = -\frac{1}{4\pi\epsilon_0}(\nabla \cdot \nabla - \frac{1}{c^2} \frac{\partial^2}{\partial t^2}) \int_V \frac{1}{|\mathbf{r} - \mathbf{r}'|} \hat{\mathbf{P}}(t - \frac{|\mathbf{r} - \mathbf{r}'|}{c}) d^3\mathbf{r}'. \quad (27)$$

Here, operator $\hat{\mathbf{P}}$ of the induced polarization describes the displacement current induced by the soliton's profile, which may be considered as an external source, from point of view of the antenna. The onsite polarization operator, written in terms of creation-annihilation operators is

$$\hat{\mathbf{P}}_{p,q}(t) = \mu \hat{\sigma}_{p,q}^+(t) + \text{H.c.} \quad (28)$$

Due to the smallness of the field produced by the soliton in the QD array, its emission is determined by the linear approximation, hence the total field is built as a superposition of partial fields emitted by different QDs independently. The plane-wave drive is, thus,

$$\begin{aligned} \hat{\mathbf{E}}(\mathbf{r}, t) = & -\frac{V}{4\pi\epsilon_0} \left(\nabla \cdot \nabla - \frac{1}{c^2} \frac{\partial^2}{\partial t^2} \right) \mathbf{e}_z \\ & \times \sum_{p=-N_1/2}^{N_1/2} \sum_{q=-N_2/2}^{N_2/2} \frac{\hat{P}_{zp,q}(t - c^{-1}|\mathbf{r} - \mathbf{e}_x pa - \mathbf{e}_y qa|)}{|\mathbf{r} - \mathbf{e}_x pa - \mathbf{e}_y qa|}. \end{aligned} \quad (29)$$

To obtain the observable value of field, it is necessary to replace the polarization operator by its main value with respect to the quantum state (12), $\langle \Psi | \hat{P}_{zp,q} | \Psi \rangle$. The result is

$$P_{zp,q}(t) = \langle \hat{P}_{zp,q}(t) \rangle = \frac{\mu}{V} \Psi_{p,q}(t) \Phi_{p,q}^* \exp[i(p\phi_1 + q\phi_2)] \exp(-i\omega t) + \text{c.c.} \quad (30)$$

It is convenient to present the far-zone field in the spherical coordinates with the origin set at the central point of the cell with $p = q = 0$, defined as $x = R \sin(\theta) \cos(\varphi)$, $y = R \sin(\theta) \sin(\varphi)$, $z = R \cos(\theta)$. The terms of order $O(R^{-2})$ should be omitted, and the radial (longitudinal) component of the electric field vanishes too. As a result, we obtain, for the quasi-spherical observable field:

$$\mathbf{E}_{\text{Rad}} = \lim_{R \rightarrow \infty} \mathbf{E} = \frac{\mu \mathbf{e}_\theta}{4\pi\epsilon_0} \frac{\omega^2}{c^2} \frac{e^{-i\omega(t-R/c)}}{R} F\left(\theta, \varphi, \phi_1, \phi_2; t - \frac{R}{c}\right) + \text{c.c.}, \quad (31)$$

with the radiation pattern

$$\begin{aligned} F(\theta, \varphi, \phi_1, \phi_2; t - \frac{R}{c}) = & \sin \theta \sum_{p=-N_1/2}^{N_1/2} \sum_{q=-N_2/2}^{N_2/2} \Psi_{p,q}(\tilde{t}) \Phi_{p,q}^*(\tilde{t}) \\ & \times \exp\left\{ip \left[\frac{\omega a}{c} \sin \theta \cos \varphi + 2\phi_1\right] + iq \left[\frac{\omega a}{c} \sin \theta \sin \varphi + 2\phi_2\right]\right\}, \end{aligned} \quad (32)$$

where $\tilde{t} \equiv t - R/c + c^{-1} \sin \theta [p \cos \varphi + q \sin \varphi]$. We stress that, in contrast with classical macroscopic antennas, the radiation pattern given by Eq. (32) is non-steady, as it exhibits a slow dependence on the spatiotemporal variable, $t - R/c$, which corresponds to the amplitude and frequency modulation of the field due to the time dependence of

probability amplitudes in quantum state (12). The stable soliton produces, through Eq. (32), a radiation pattern in the form of

$$F(\theta, \varphi, \phi_1, \phi_2) = \sin \theta \sum_{p=-N_1/2}^{N_1/2} \sum_{q=-N_2/2}^{N_2/2} A_{p,q} B_{p,q}^* \exp \left\{ ip \left[\frac{\omega a}{c} \sin \theta \cos \varphi + 2\phi_1 \right] \right\} \\ \times \exp \left\{ iq \left[\frac{\omega a}{c} \sin \theta \sin \varphi + 2\phi_2 \right] \right\}. \quad (33)$$

In particular, the radiation pattern produced by the 1D in the 2D space can be written in a simple form by setting $N_2 = 0$ in Eq. (33):

$$F(\theta, \varphi, \phi) = \sin(\theta) \sum_{p=-N/2}^{N/2} A_p B_p^* \exp \left\{ ip \left[\frac{\omega a}{c} (\sin \theta) (\cos \varphi) + 2\phi \right] \right\}, \quad (34)$$

where the notation is changed as $A_{p,q} \rightarrow A_p$, $B_{p,q} \rightarrow B_p$, $\phi_1 \rightarrow \phi$, $N_1 \rightarrow N$, to comply with that adopted in Ref. [27].

It is relevant to note that, according to Ref. [39] the radiation pattern is subject to the Onsager kinetic relations, which take into regard symmetry constraints [40]. As it follows from Eqs. (13) and (26), $(A_{-p,-q} B_{-p,-q}^*) = (A_{p,q} B_{p,q}^*)$, hence

$$F(\pi - \theta, \varphi, -\phi_1, -\phi_2) = F(\theta, \varphi, \phi_1, \phi_2), \quad (35)$$

while $F(\pi - \theta, \varphi, \phi_1, \phi_2) \neq F(\theta, \varphi, \phi_1, \phi_2)$. It shows that, rotating the QD array by 180° , one should invert the propagation direction of the driving field to keep the physical state invariant, similar to the the sign of the angular velocity in the rotating liquid, or the sign of the magnetic field [40]. This symmetry agrees with the non-reciprocity of the Rabi waves exhibited by Eq. (24).

For the cylindrical drive, the radiation pattern in the far-field zone is obtained from Eq. (31) in a similar way:

$$F(\theta, \varphi) = \sin \theta \sum_{p=-N_1/2}^{N_1/2} \sum_{q=-N_2/2}^{N_2/2} A_{p,q} B_{p,q}^* |S_{p,q}| \exp \left\{ \frac{i\omega a}{c} \sin \theta [p \cos \varphi + q \sin \varphi] \right\}. \quad (36)$$

The useful information in antenna context are the radiation patterns in the E - and H -planes defined, respectively, as $F_e(\theta) \equiv F(\theta, \varphi = \pi/2)$ and $F_h(\theta) \equiv F(\theta = \pi/2, \varphi)$ [28]. Plots of these quantities follow the corresponding dynamically stable soliton evolution in figures below.

4. Results and discussion

4.1. Rabi solitons driven by the plane wave

After stationary solitons were found as outlined above [see Eq. (26)], their stability against small perturbations was examined in the framework of linearized equations for small perturbations added to the stationary solution,

$$\Psi_{p,q}(t) = [A_{p,q} + \delta A_{p,q}(t)] e^{-i\Omega t}, \quad \Phi_{p,q}(t) = [B_{p,q} + \delta B_{p,q}(t)] e^{-i\Omega t}. \quad (37)$$

In this case, the linearization of Eq. (13) with respect to the perturbations $\delta A_{p,q}$ and $\delta B_{p,q}$, leads to a linear eigenvalue (EV) problem for the instability growth rate of small perturbations. Obviously, the soliton is stable if all the eigenvalues have zero real parts. On the other hand, the presence of EVs with a positive real part indicates at exponential or oscillatory instability, in the cases of purely real or complex EVs, respectively. Finally, the dynamical stability of the discrete solitons was verified by dint of direct simulations of Eqs. (13).

It is well known that the single-component 2D DNLS equation gives rise to three types of fundamental discrete solitons: stable onsite, and unstable hybrid and inter-site ones [49], along with several types of vortices with vorticity $S = 1$ (eight configurations) and $S = 2$ (four configurations) [49, 50, 51]. The vorticity is identified as the winding number of the phase of the lattice field, i.e., the total change of the phase along a closed curve surrounding the pivotal point of the vortex, divided by 2π . We here consider the values of $S = 1$ and $S = 2$.

Obviously, the soliton complexes must be located inside the semi-infinite gap of dispersion relation (23), see Fig. 2. The most straightforward counterpart of the single-component 2D DNLS equation is the model of the QD array based on Eq. (13) with zero detuning, $F = 0$ and $\phi_1 = \phi_2 = 0$. In this system, we find soliton complexes formed by two identical real components of the onsite, hybrid, and inter-site types (Fig. 3), and families of discrete vortex solitons with topological charges $S = 1$ and $S = 2$ (together with quadrupoles), which are supported by the attractive XPM interaction. The localized modes in each component are similar to the corresponding types of fundamental and vortex solitons formed in the single-component 2D DNLS equation.

Different types of vortices in each component are schematically shown in tables I and II. Configurations a, c, d, e, f, g, i , and j represent possible structures of onsite vortices, with the pivotal point located on a lattice site, while b, h, k , and l generate off-site vortices, whose pivot falls located between lattice sites (the same nomenclature as in Ref. [50]). An example of the vortex of type a is plotted in Fig. 4.

The linear-stability analysis shows that the complexes formed by identical fundamental-soliton onsite components are stable, and that there are stability regions in the respective parameter space for vortex configurations of types a, b (ground-state vortices), e, g with $S = 1$ (excited state vortices), as well as for types j, k with $S = 2$. The corresponding radiation-field distributions for the onsite fundamental solitons are plotted in Fig. 5, while the same for the stable vortices of the a and b types is shown in Fig. 4. The vortices of type k actually feature an offsite quadrupole configuration (rather than a truly vortical one), based on the four-site frame and sharp phase changes in steps of π between lattice sites. The stability regions of all the above-mentioned complexes almost overlap with the stability regions of their counterparts in the single-component 2D DNLS equation. Briefly speaking, the vortex-stability range is narrow, particularly for spatially broad vortices, and shrinks with the increase of ξ (which is the counterpart of the inter-site coupling constant C in single-component DNLS equation [50]). This is in accordance with the fact that large ξ corresponds to the continuum

limit, in which all the localized vortex modes are unstable. We have also checked a possibility to form vortex complexes formed of two identical vortices with opposite signs (phase shift π), but they all turn out to be unstable.

The predicted dynamical stability and instability has been confirmed by direct simulations for the onsite fundamental soliton complexes and certain vortex complexes for typical values of the system's parameters. The onsite fundamental complexes and those vortex complexes which were predicted to be stable indeed keep their amplitude and phase structure (i.e., the vorticity) in the course of the evolution. On the other hand, hybrid and offsite complexes, whose instability is predicted by the linear-stability analysis, radiate away a significant part of their norm and rearrange into dynamically robust onsite-centered localized breathers. Direct simulations of vortex complexes, which were predicted to be unstable, demonstrate that their amplitude profiles are quite robust, and they keep the vorticity in the course of the evolution. However, the symmetry with respect to the pivot is broken, and the symmetry between their two components is broken too. The so established mode may be categorized as an irregularly oscillating vortex breather, see Fig. 6.

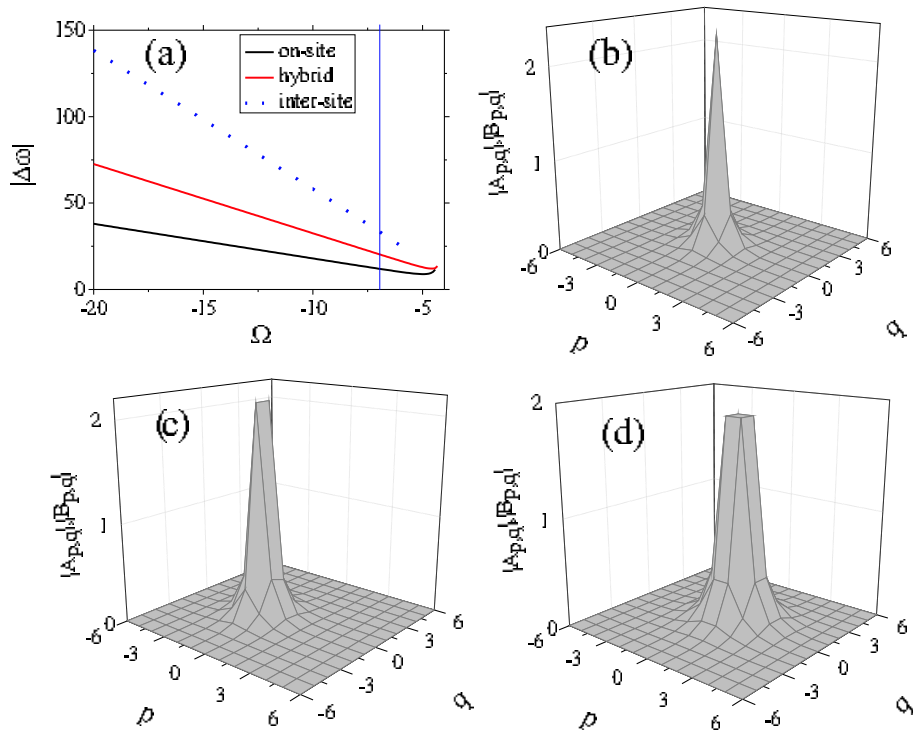


Figure 3. Families of fundamental solitons, formed by two identical onsite (solid black line), hybrid (solid red line) and offsite (dotted green line) components, are represented by the corresponding $|\Delta\omega(\Omega)|$ dependencies in (a). Examples of these solitons for $\Omega = -7$ [the vertical blue line in (a) which intersects all three curves] are shown in (b) – onsite, (c) – hybrid and (d) – offsite, respectively. This figure pertains to the model with the plane-wave excitation, see Eq. (13).

In the 2D array of QDs with nonzero detuning ($F = 1$ is chosen below, as a characteristic example), all types of the above-mentioned fundamental and vortical

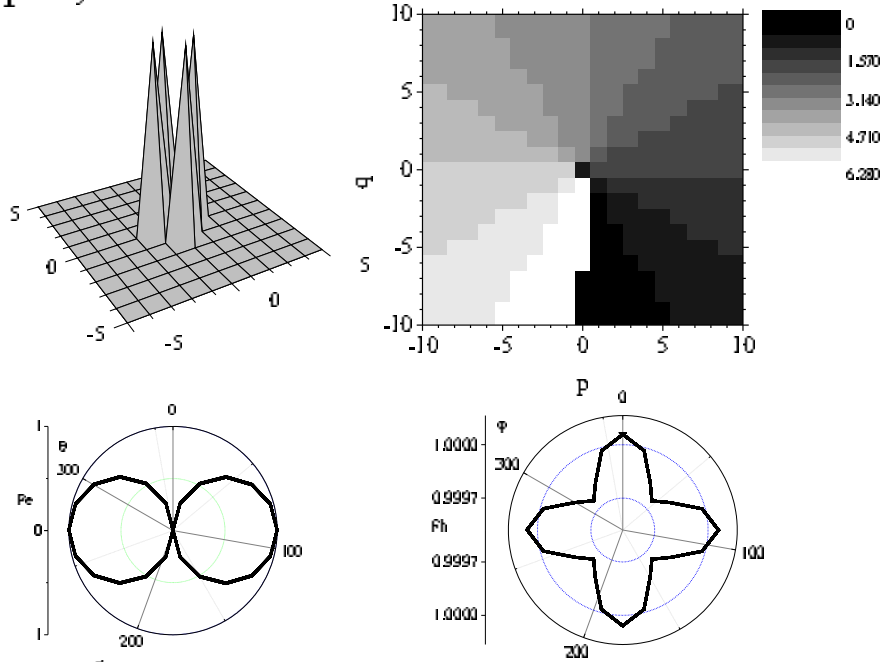
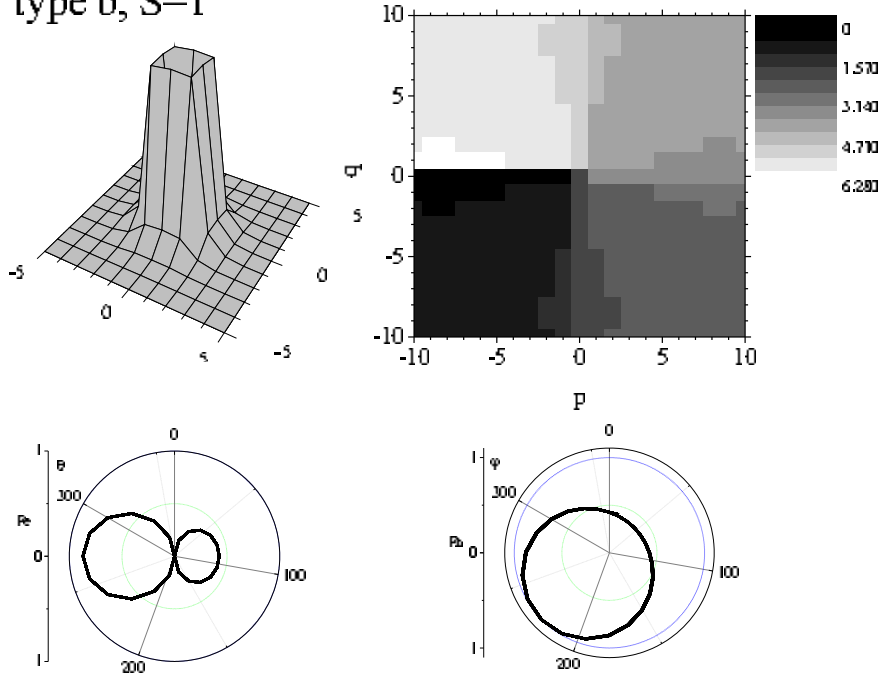
type a, $S=1$ type b, $S=1$ 

Figure 4. Amplitude, phase profiles, and radiative patterns in E - and H -planes of vortices with $S = 1$ defined as types a and b in Ref. [51]. The parameters in Eq. (13) are $\xi = 0.01$, $F = 0$, $\phi_1 = \phi_2 = 0$, and $\Omega = -19.3$. Both are stable according to the linear-stability analysis and dynamical simulations.

complexes can be generated, but the symmetry between the two components ($A_{p,q}$ and $B_{p,q}$) is not preserved. Simultaneously, the similarity to the single-component DNLS equation is lost. Namely, the overall shape of the components in fields $A_{p,q}$ and $B_{p,q}$ is kept, but amplitudes and widths of the components change, and their precise symmetry

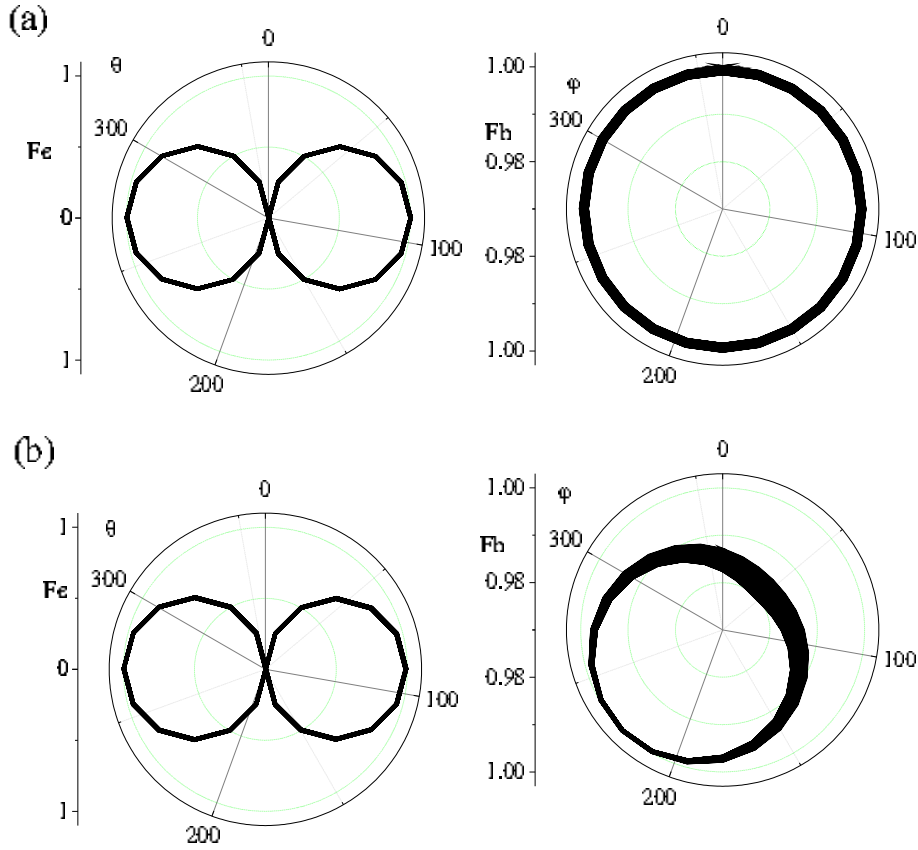


Figure 5. The radiative patterns in the E - and H -directions, $F_e(\theta)$ and $F_h(\phi)$, for the complex consisting of two fundamental onsite solitons with (a) $\Omega = -7$, $F = 0$, $\phi_1 = \phi_2 = 0$ and (b) $\Omega = -7$, $F = 0$, $\phi_1 = \phi_2 = \pi/4$. The plane-wave excitation is considered, see Eq. (13).

about the central point is broken (slightly violated). In this case, the linear-stability analysis does not predict the existence of genuinely stable fundamental complexes, with the exception of the vortex complexes of type a , with $S = 1$, and of type k , with $S = 2$, see below. However, dynamical simulations demonstrate that localized modes of the onsite type form robust breathing complexes, which keep the initial overall structure (in particular, the vorticity is kept).

On the other hand, the computation of the eigenvalues for small perturbations shows stability of vortex complexes of type a , with $S = 1$, as well as of types k with $S = 2$ in the presence of $F \neq 0$. Dynamical simulations confirm their stability in the corresponding parameter regimes. Other families of vortex complexes formed at $F \neq 0$ are unstable according to both the linear-stability analysis and dynamical simulations. In fact, the instability destroys their phase structure, while the amplitude patterns remain quite robust.

Thus, the general conclusion concerning the system (13) driven by the plane wave is that, in the absence of the phase shifts, $\phi_1 = \phi_2 = 0$, the stability of the complexes is similar to what is known about their counterparts in the single 2D DNLS equation single 2D lattice case. Namely, irrespective of the presence of the detuning, F , in Eq. (13),

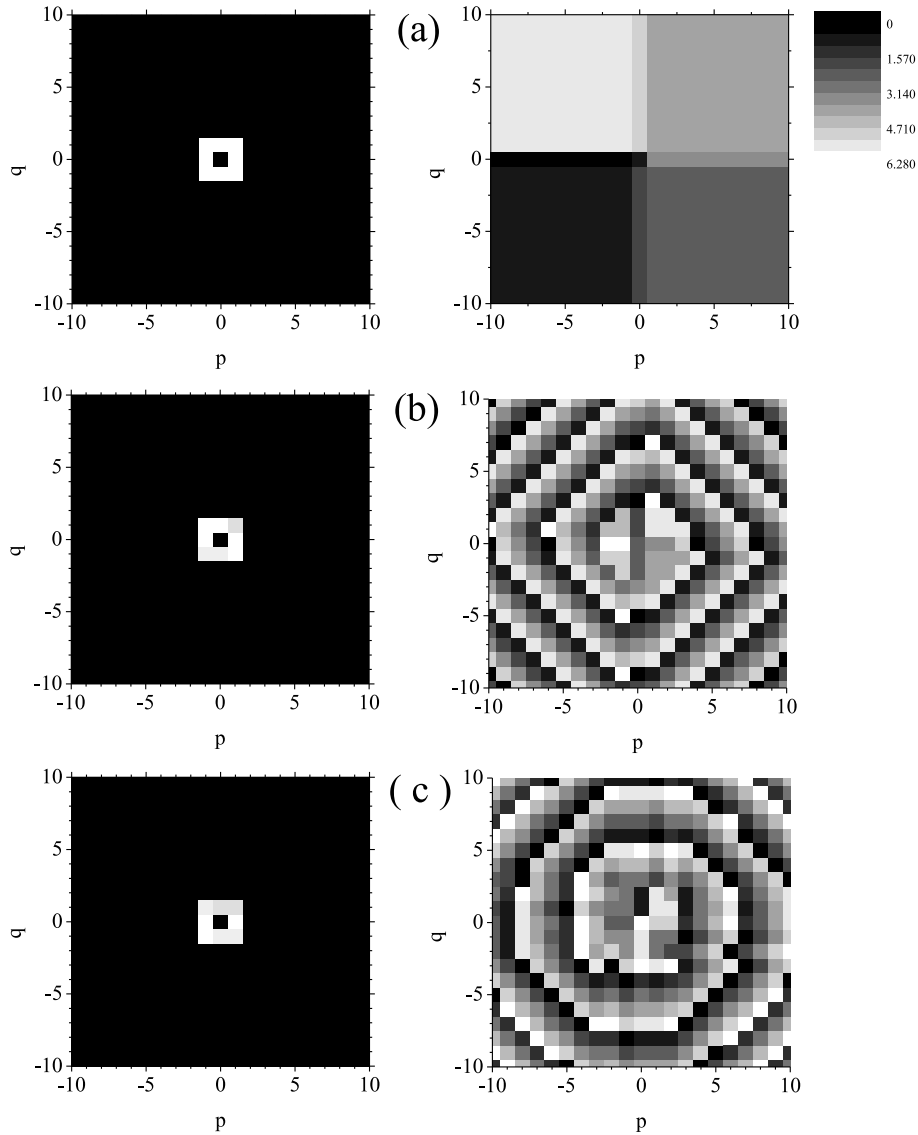


Figure 6. The evolution of one component of an unstable vortex of type c with $S = 1$. (a) The amplitude and phase profiles of the stationary vortex with $\Omega = -10$. Panels (b) and (c) show the profiles in the course of the perturbed evolution ($t = 50$ and $t = 100$ in arbitrary units, respectively). Other parameters are $\xi = 0.01$, $F = 0$, $\phi_1 = \phi_2 = 0$.

the those modes which were stable in the single-component model, remain completely or effectively stable in the two-component one, evolving in some cases from the stationary shapes into breathing ones, but keeping the overall structure.

Considering the system with non-zero phase shifts, ϕ_1 and ϕ_2 in Eq. (13), we mainly focus on two configurations, *viz.*, the diagonal and anisotropic ones, with $\phi_1 = \phi_2 = \pi/4$ or $\phi_1 = 0$, $\phi_2 = \sqrt{2}\pi/4$, respectively. In both these cases, we have found complexes of all the above-mentioned types. Namely, fundamental solitons of the onsite, hybrid and inter-site types, with symmetric components, in the case of $F = 0$ (see Fig. 7), and their asymmetric counterparts at $F \neq 0$. The existence boundary for the fundamental soliton complexes is slightly altered by the nonvanishing phase shifts, as can be seen

from small changes of the respective dispersion surfaces displayed in Fig. 2. Example of the soliton radiation fields for a stable configuration is shown in Fig. 5(b).

Counterparts of all the vortex field configurations, which are identified above in the system with $\phi_{1,2} = 0$, are also found in the system with $\phi_{1,2} \neq 0$. Differences are observed in the boundary of the existence region, and parameter regions where robust vortex breathers appear. In Fig. 8, the evolution of the symmetric vortex soliton of type *a* is displayed for $\phi_1 = \phi_2 = \pi/4$, $F = 0$. According to the computation of perturbation eigenvalues, stable complexes of two *a* type vortices (with topological charge $S = 1$) keep their stability at $\phi_1 = \phi_2 \neq 0$, while unequal phase shifts destabilize the complexes. The radiation pattern keeps its shape, as shown in Fig. 8(c). Most robust are complexes formed by the quadrupoles of type *k* with $S = 2$, in the sense that they are stable in a certain parameter area for all relations between phases ϕ_1 and ϕ_2 . Lastly, the phase differences always destabilize other types of vortex complexes. In general, the value of the corresponding instability rate, which is proportional to a purely real eigenvalue, increases with increasing ϕ_1 , ϕ_2 and fixed F . Direct simulations confirm that only complexes formed by the onsite fundamental solitons, and certain types of vortices are stable in particular parameter ranges, chiefly in the form of robust localized breathing patterns. Similar to what is mentioned above, the instability destroys the phase structure of vortices, without essentially affecting the amplitude pattern.

Thus, we conclude that the changes in values of phase shifts $\phi_{1,2}$ in Eq. (13), which are introduced by the oblique incident plane waves, as well as the detuning, F , do not cause qualitative changes in the structure and effective stability of the 2D self-trapped fundamental modes and particular types of vortex complexes, of type *a* with $S = 1$, and type *k* with $S = 2$ (the quadrupole). Finally, systematic simulations demonstrate that moving discrete-soliton complexes cannot be found in the present 2D model.

4.2. Rabi solitons driven by the cylindrical wave

For the 2D QD array with the cylindrical-wave excitation, described by Eq. (19), we report here results obtained for $ka = \pi/4$. As we shown by detailed analysis, these results adequately represent the generic situation.

Similar to the planar-wave model, soliton complexes are located in the semi-infinite gap in the linear spectrum. However, unlike Eq. (23), the spectrum with the cylindrical driving wave cannot be found analytically, therefore it was calculated numerically. Two-component fundamental solitons are built, as above, of two components, each of them being of the onsite, inter-site, or hybrid type. Vortex complexes found in the present system are displayed in Fig. 9. These are complexes of *b* and *l* types with $S = 1$, or of *k* and *h* types with $S = 2$, see Tables I and II. In the system with a nonzero detuning parameter $F \neq 0$, all types of the above-mentioned fundamental and vortical complexes are generated, but the symmetry between the two components is not preserved.

The linear-stability analysis shows that the complexes formed identical fundamental-soliton onsite components are stable for all value of detuning F , and there

Table 1. Schemes of the amplitude and phase profiles corresponding to the two identical components of the discrete vortex with $S = 1$ in the system with $F = 0$, $\phi_1 = \phi_2 = 0$ [the model with the plane-wave excitation, Eq. (13)]. Explicitly written shares of π (or 0) are values of the phase at main sites carrying the vortex complex. Symbol x designates sites with zero amplitude. Only complexes with the components of the b and l types for $S = 1$, and of the k and h types for $S = 2$, respectively, are found in the model with the cylindrical-wave excitation.

Type	S	Phase configuration	Stable (plane wave/ cylindrical wave)
a	1	$\begin{array}{c} 0 \\ \pi/2 \quad x \quad 3\pi/2 \\ \pi \end{array}$	Yes/No
b	1	$\begin{array}{c} 0 \quad 3\pi/2 \\ \pi/2 \quad \pi \end{array}$	Yes/No
c	1	$\begin{array}{c} \pi/4 \quad 0 \quad 7\pi/4 \\ \pi/2 \quad x \quad 3\pi/2 \\ 3\pi/4 \quad \pi \quad 5\pi/4 \end{array}$	No/No
d	1	$\begin{array}{c} 0 \\ \pi/4 \quad x \quad 7\pi/4 \\ \pi/2 \quad x \quad x \quad x \quad 3\pi/2 \\ 3\pi/4 \quad x \quad 5\pi/4 \\ \pi \end{array}$	No/No
e	1	$\begin{array}{c} 0 \\ \pi/4 \quad x \quad 7\pi/4 \\ \pi/2 \quad x \quad 0 \quad x \quad 3\pi/2 \\ 3\pi/4 \quad x \quad 5\pi/4 \\ \pi \end{array}$	Yes/No
f	1	$\begin{array}{c} 0 \\ \pi/4 \quad 0 \quad 7\pi/4 \\ \pi/2 \quad \pi/2 \quad x \quad 3\pi/2 \quad 3\pi/2 \\ 3\pi/4 \quad \pi \quad 5\pi/4 \\ \pi \end{array}$	No/No
g	1	$\begin{array}{c} 0 \\ \pi/4 \quad \pi \quad 7\pi/4 \\ \pi/2 \quad 3\pi/2 \quad x \quad \pi/2 \quad 3\pi/2 \\ 3\pi/4 \quad 0 \quad 5\pi/4 \\ \pi \end{array}$	Yes/No
h	1	$\begin{array}{c} 0 \quad 7\pi/4 \\ \pi/4 \quad 0 \quad 3\pi/2 \quad 3\pi/2 \\ \pi/2 \quad \pi/2 \quad \pi \quad 5\pi/4 \\ 3\pi/4 \quad \pi \end{array}$	No/No

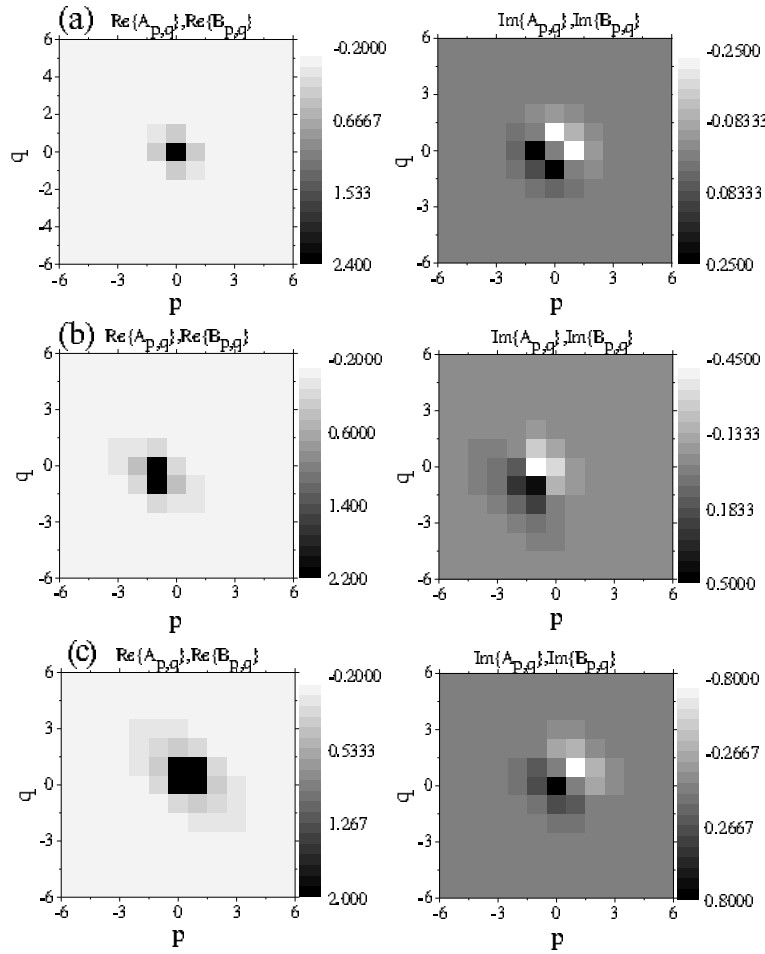


Figure 7. Examples of fundamental-soliton complexes [in the model with the plane-wave excitation, Eq. (13)], formed by identical components, at $F = 0$, $\Omega = -7$, and $\phi_1 = \phi_2 = \pi/4$. Plotted are real and imaginary parts of the stationary lattice fields for the complexes of the onsite (a), hybrid (b), and intersite (c) types, respectively.

are stability regions in the respective parameter space for vortex configuration of type k with $S = 2$ at $F = 0$. The stability region of latter mode almost overlaps with its counterpart for the corresponding vortex complex in the 2D system with the plane-wave excitation. Radiation patterns of stable solitary Rabi structures excited by the cylindrical wave are plotted in Fig. 11.

The predicted dynamical stability has been confirmed by direct simulations for the onsite fundamental soliton complexes (Fig. 10) and vortex complexes for particular values of the system parameters. Similar to what was seen above, stable vortices preserve their amplitude and phase patterns, as shown in Fig. 12. In general, effectively stable localized patterns (including those which are unstable in terms of the eigenvalues but exhibit persistence in direct simulations) evolve as breathing modes. In contrast, the unstable hybrid and inter-site complexes radiate into background a significant part of their energy. The remaining energy can be reorganized as a new localized onsite breathing structure, see Fig. 13. On the other hand, unstable vortex complexes are

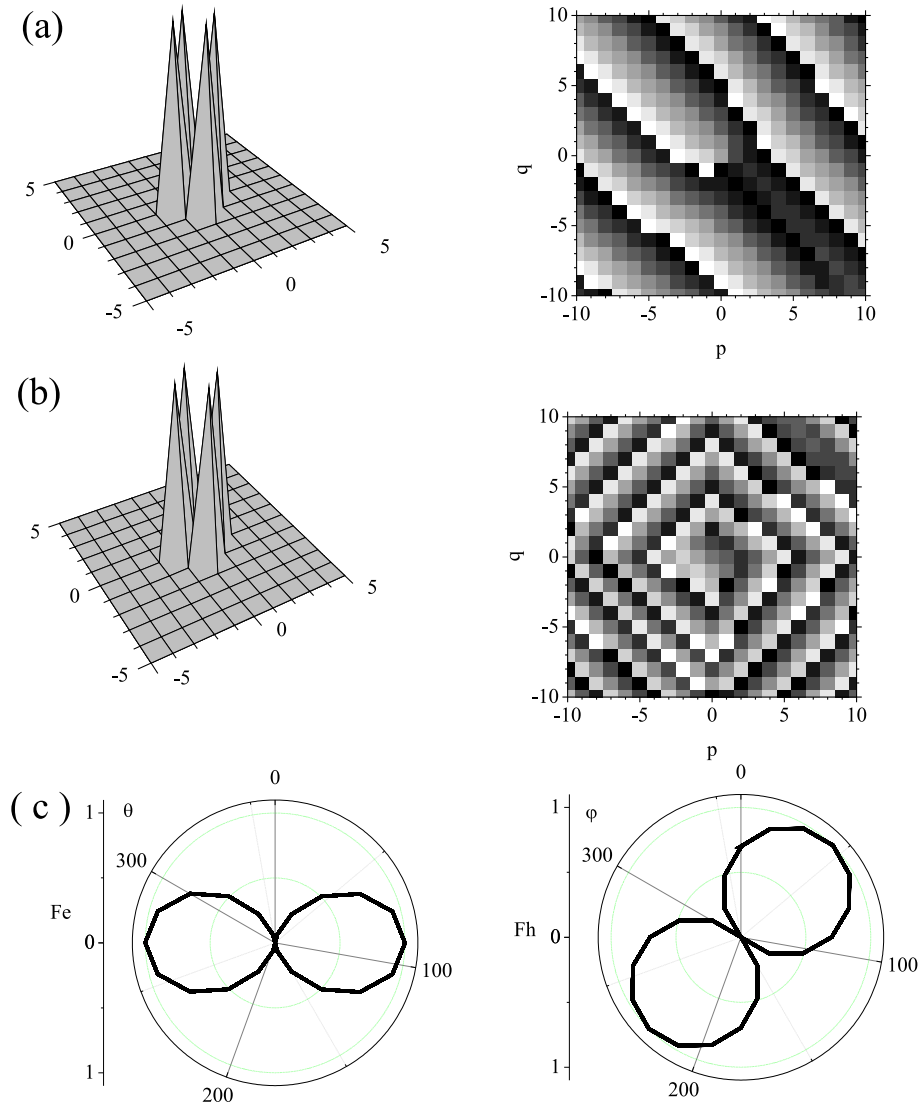


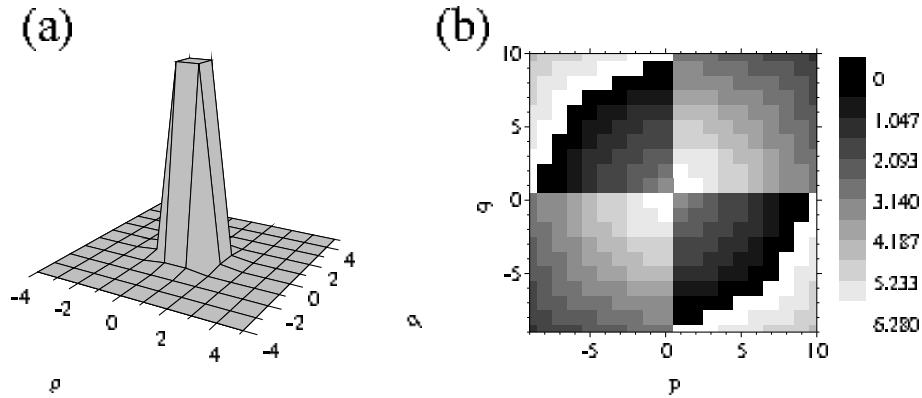
Figure 8. Initial (a) amplitude and phase profiles of the vortex of type a , in terms of Ref. [51], the result of its evolution at $t = 100$ (b), and the respective radiative patterns F_e and F_h (c). The parameters in Eq. (13) are $\xi = 0.01$, $F = 0$, $\phi_1 = \phi_2 = \pi/4$, and $\Omega = -18$.

more robust structures with significantly reduced radiation of energy to the background. The newly formed breathing structures preserve localization but phase coherence is destroyed. The symmetry of the profile with respect to the center of vortex is broken, as well as the symmetry between the components, see Fig. 14.

In the physical system underlying the present lattice model, parameters may be known only with a finite accuracy, which makes it necessary to test the stability of the localized modes with respect to random variations of coefficients of Eqs. (13) and (19). We have performed this test by introducing random changes, of relative amplitude 10%, of coefficients ξ and F , which represent uncertainties in QD energy levels, and tunneling matrix elements that determine the strength of the inter-site coupling. The

Table 2. Schemes of the amplitude and phase profiles corresponding to vortex solitons with $S = 2$.

Type	S	Phase configuration	Stable (plane wave/cylindrical wave)
i	2	$\pi/2$ 0 $3\pi/2$ π x π $3\pi/2$ 0 $\pi/2$	No/No
j	2	0 $\pi/2$ x $3\pi/2$ π x x x π $3\pi/2$ x $\pi/2$ 0	Yes/No
k	2	0 π π 0	Yes/Yes
l	2	0 $3\pi/2$ $\pi/2$ 0 π π π π 0 $\pi/2$ $3\pi/2$ 0	No/No

**Figure 9.** The amplitude (a) and phase (b) patterns of the vortex in each component of the complex of the k type with $S = 2$, excited by cylindrical wave.

result (not shown here in detail) is that all the localized modes which were found above to be dynamically stable are also structurally stable against the random variations of the system's parameters. In fact, the robustness of discrete solitons against random deformations of the underlying lattices is known in earlier studied models [6].

The bottom line of this subsection is that in the system with the cylindrical-wave excitation, fundamental onsite soliton complexes and vortical ones of the k type with $S = 2$ are stable in certain areas of their existence region. In addition, we point out that the soliton-produced radiation patterns may be used as digital signals for data coding in the framework of the quantum information transition. Due to the different patterns of these signals for different types of the models, driven by the plane and cylindrical waves, they may be identified clearly.

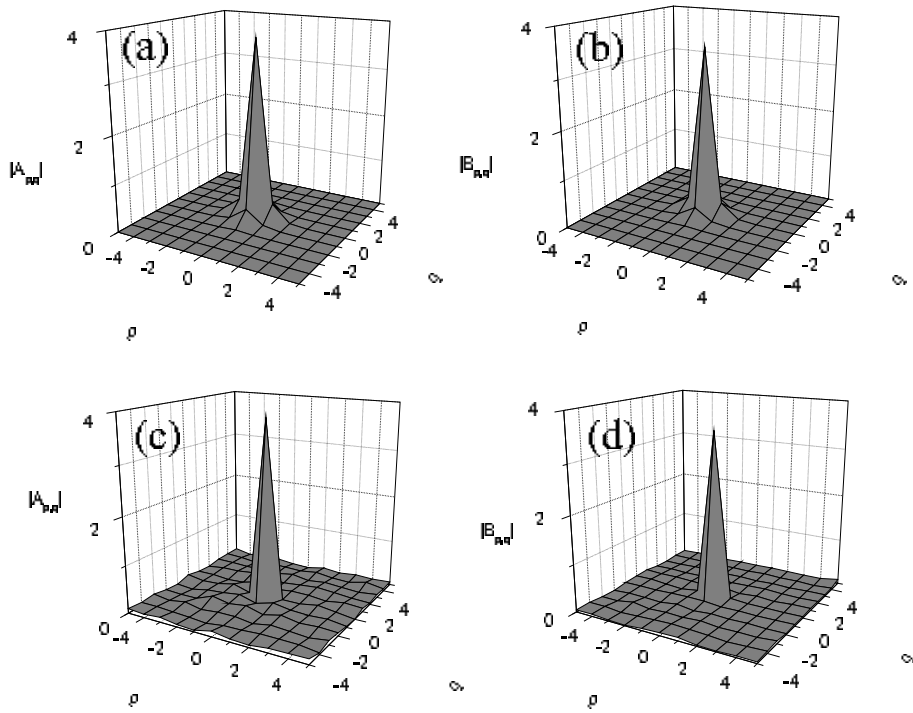


Figure 10. The evolution of the amplitude pattern of the onsite soliton complex with $\mu = -17$, $\Delta\omega = -30$, $F = 1$ in the model with the cylindrical-wave excitation, see Eq. (19). Plots correspond to $t = 0, 50, 100$ presented in arbitrary units.

4.3. The concept of solitonic nano-antennas

As said above, the transmitting antenna is defined as a device which converts the near field into the far field [28]. On the other hand, the Rabi solitons feature the spatially distributed polarization induced by the RO, as seen in Eqs. (28) and (30). The 2D electromagnetic radiation patterns induced by these polarization profile suggest to consider the present system in the context of the realization of transmitting antennas. Thus, the Rabi soliton offers a previously unexplored physical mechanism to emulate the antennas, while the driving field plays the role of the external energy source launching and driving this device.

For the data transfer, the emitted field should be temporally modulated by an input signal through the driving electromagnetic field. Actually, this modulation is relatively slow, hence it may be considered as an adiabatic process. As mentioned above, a basic characteristic of the antenna is the 2D radiation pattern, or, in some cases, partial patterns in the E - and H -planes [28]. The necessity to consider the radiation profiles in 2D makes the present analysis principally different from the study of RO solitons in 1D arrays, which was recently reported in Ref. [27].

Radiation pattern (33) produced by the QD array can be rewritten in terms of the standard notation adopted in the antenna theory [28] as $F(\theta, \varphi) = \sin(\theta) \cdot (AF)_{N_1 \times N_2}$. The first factor, $\sin(\theta)$, is the radiation pattern of a single emitter (in our case, the

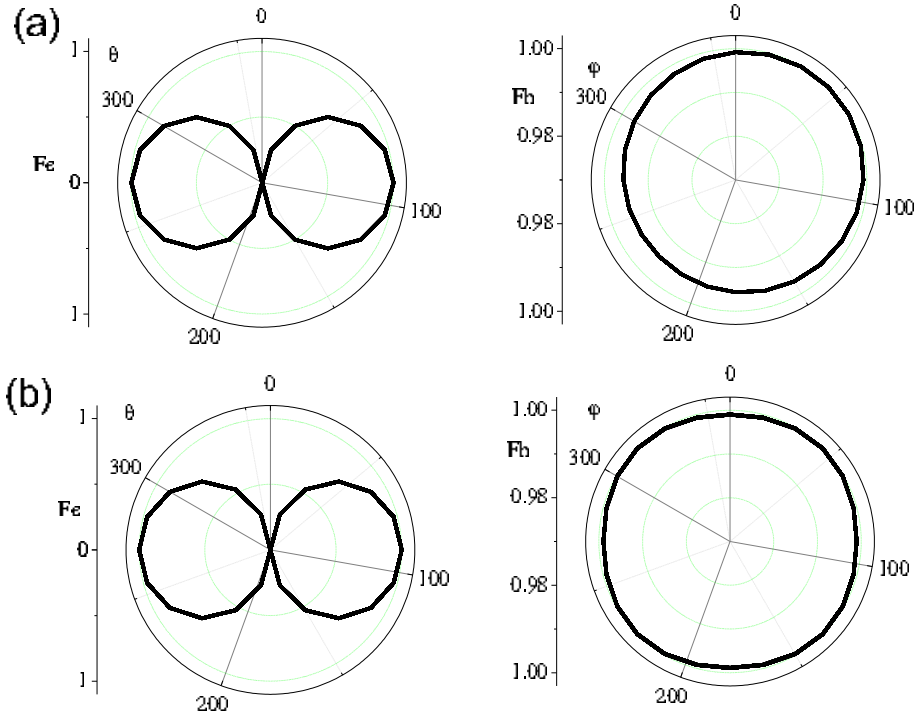


Figure 11. Radiation patterns F_e and F_h for (a) the onsite complex with $\mu = -17$, $\Delta\omega = -30$, $F = 1$, and (b) the vortical complex of the k type with $F = 0$, $\mu = 17.2$, $S = 2$, in the model with the cylindrical-wave excitation, Eq. (19).

electric dipole), while the second one is the array factor,

$$(AF)_{N_1 \times N_2} = \sum_{p=-N_1/2}^{N_1/2} \sum_{q=-N_2/2}^{N_2/2} A_{p,q} B_{p,q}^* \exp \{ip [c^{-1}\omega a (\sin \theta) (\cos \varphi) + 2\phi_1]\} \\ \times \exp \{iq [c^{-1}\omega a (\sin \theta) (\sin \varphi) + 2\phi_2]\}. \quad (38)$$

In the macroscopic phased antenna array, elements are excited by a signal having a constant amplitude and the phase which uniformly increases along the array's axis [28]. The array factor for that case corresponds to Eq. (38) with $A_{p,q} B_{p,q}^* = 1$. The phase variation allows one to perform scanning of the space by turning off the main lobe of the radiation pattern. One of the most efficient means to implement the antenna control is the use of switched-beam systems which can impose different angular patterns, in order to enhance the emitted signal in a preferable direction. The beam-forming algorithm is implemented through a complex pattern of the excitation of individual elements [which corresponds to factor $S_{pq} = A_{p,q} B_{p,q}^*$ in notation (38)], adjusted so as to place the maximum of the main beam in the necessary direction [28].

The purport of the solitonic nano-antenna concept is to introduce the beam-forming algorithm, which is determined by the set of factors S_{pq} , using the soliton-emission profile. As several different stable solitons may exist in the given array, the choice of the overall profile depends on initial conditions. This implies that a finite number of predefined array factors exist for a given set of antenna parameters, while the initial

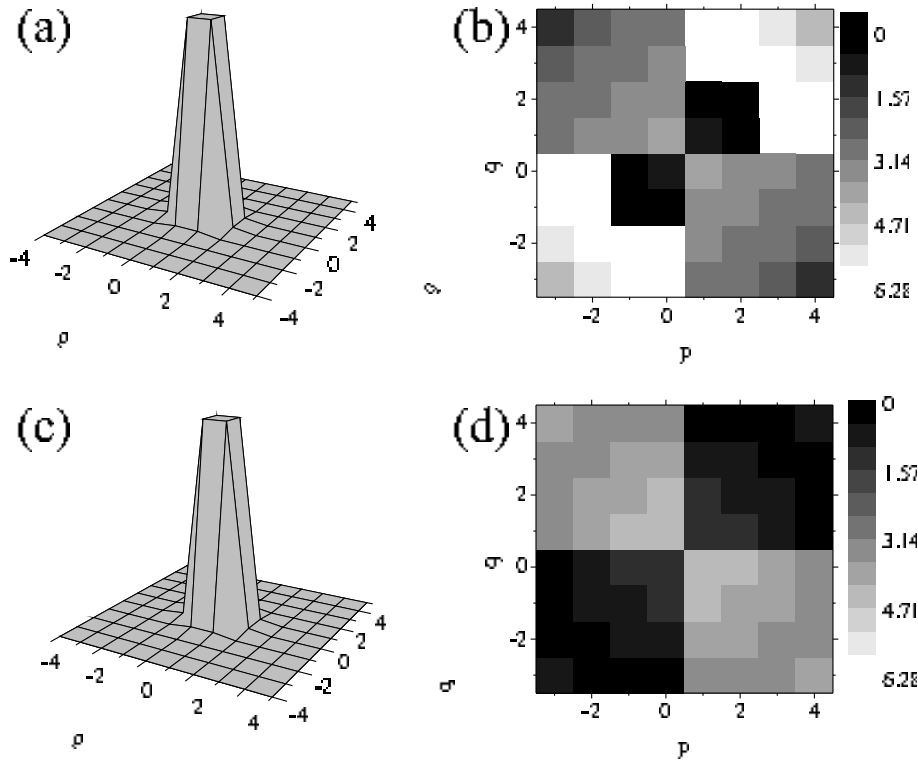


Figure 12. The evolution of the stable vortex complex of the k type, excited by the cylindrical wave, is illustrated by amplitude and phase patterns, shown at two moments of time. Parameters are $F = 0, \mu = 17.2, S = 2$. Plots correspond to $t = 0$ and 50 in arbitrary units.

conditions give a facility for choosing and switching the suitable one. To the best of our knowledge, this feature has no analogs in previously developed types of nano-antennas, and it seems quite promising from the practical point of view.

For the stable solitons built of two identical components, A and B in terms of Eq. (22), the array-factor pattern is independent on the phase profile of the soliton. Partial radiation patterns in the E - and H -planes for different types of the solitons and different types of the excitation are displayed in Figs. 4, 5, 8, and 11.

A basic problem that one should take care of to implement emitting nano-arrays in the real physical setting is maintaining the coherence of individual emitters in the array over sufficiently long time. The destruction of the coherence is contributed to by physical mechanisms of dephasing and relaxation, as well as by material imperfections of the underlying array. Recent experimental results clearly demonstrate that these problems may be resolved, allowing quite large QD arrays to maintain the coherent behavior even at room temperatures [52, 53].

There are two types of QDs that are commonly employed in nanophotonics [54]. The first one is built of semiconductor nanocrystals (typically II-IV compounds) embedded in a glass matrix. In Ref. [52], the QD ensemble of the CdSe/ZnS core/shell nanocrystals, capped with octade-cylamine, has been produced. It was fabricated as a

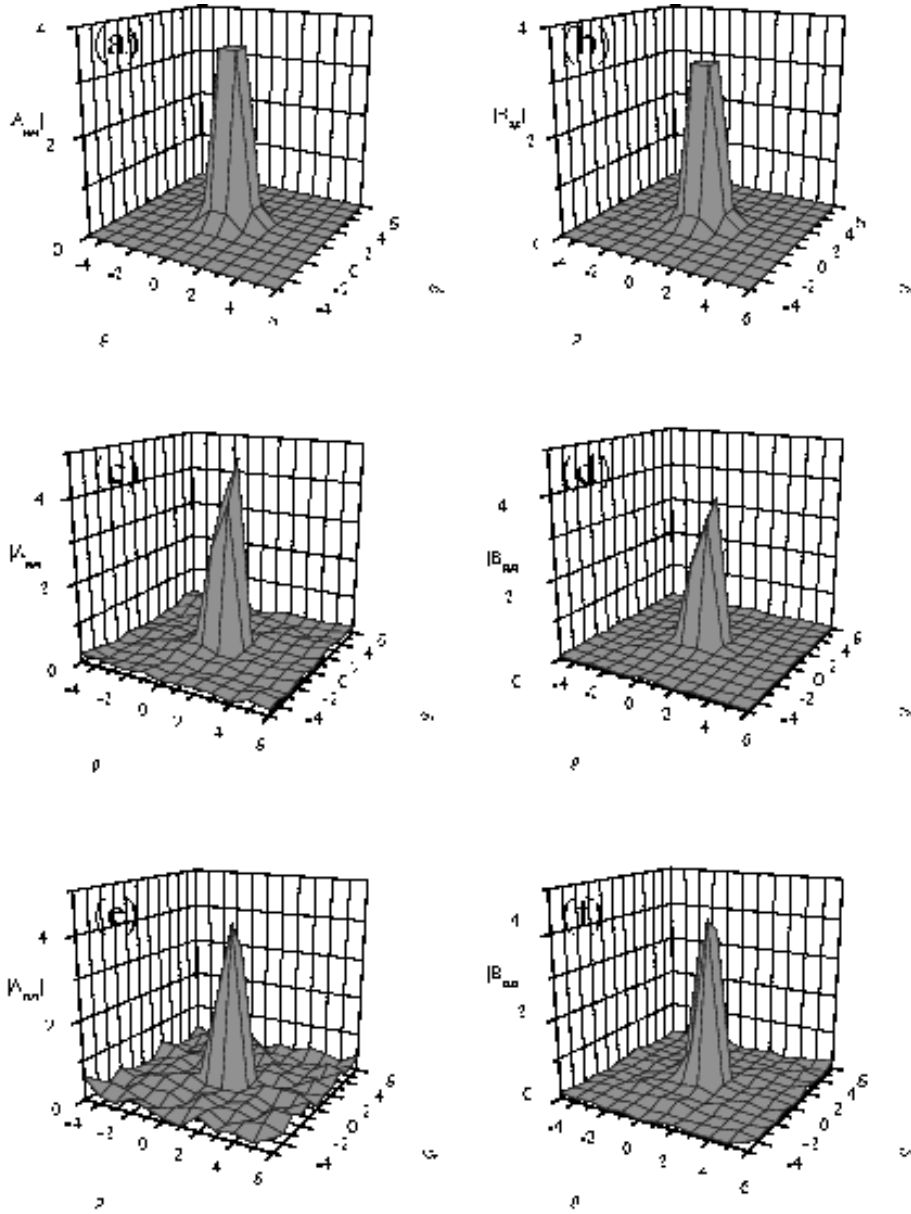


Figure 13. The perturbed evolution of the amplitude pattern of an offsite soliton, for $\mu = -17$, $\Delta\omega = -110$, $F = 1$. The cylindrical-wave excitation is used, see Eqw. (19). Plots correspond to $t = 0, 50, 100$ in arbitrary units.

2D inhomogeneously broadened close-packed network of 50×50 sites, with the average diameter and interdot distance 5.2 and 7.9nm, respectively. There also appeared dark QDs associated with defects in the ensemble. The qualitative picture of the exciton dynamics in the QD array observed in Ref. [52], based on direct measurements, shows that when an exciton is photoexcited in a high-energy QD, energy transfer occurs preferentially to a low-energy QD. At low temperatures, the exciton is trapped at a local low-energy site to which the energy was transferred. In contrast to that, at room temperature the exciton hops repeatedly, until it is transferred to a dark QD, where it undergoes nonradiative recombination. When an exciton is photoexcited in a low-

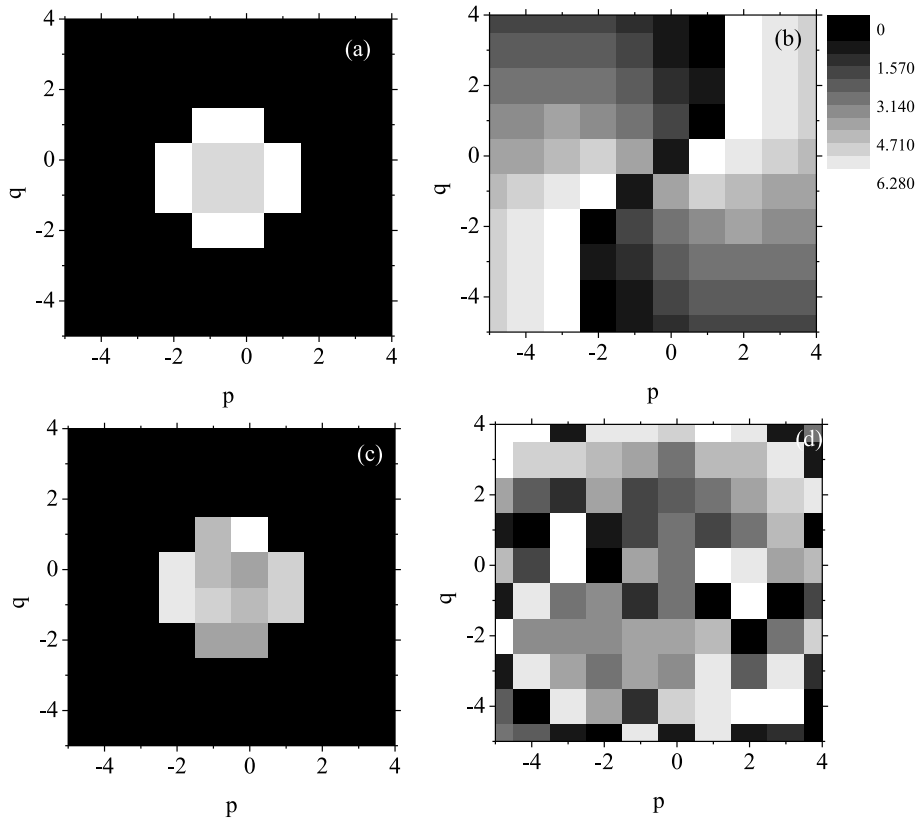


Figure 14. The evolution of an unstable vortex of the l type in the model with the cylindrical-wave excitation. Parameters are $F = 0, \mu = 17.2, S = 1$. Plots correspond to $t = 0$ and $t = 100$ in arbitrary units.

energy QD, it tends to be trapped in it. However, at room temperature, there is a non-negligible probability for the exciton to be transferred from a lower-energy QD to a higher-energy one. In Ref. [52], time- and spectrally resolved fluorescence intensities were measured by means of site-selective spectroscopy at both room and low (80 K) temperatures. The respective inverse radiative decay rate is found to be 15 ns, which makes such type of arrays promising for the implementation of nano-antennas.

The second type of QDs is the self-organized structures produced by the epitaxial crystal growth in the Stranski-Krastanov regime [54]. The self-assembled QD array was grown in Ref. [53] with the help of the molecular-beam epitaxy on a semiconducting (100)-oriented GaAs background, with a 500 nm N^+ -GaAs buffer layer. The respective lens-shaped $In_{0.65}Al_{0.35}As$ quantum dot is a part of a sphere with a fixed height of 3.4 nm and base diameter of 38 nm. The photoluminescence spectrum of the QD array is time-resolved at the excitation density of 1065 W/cm^2 , at 77 K. The corresponding exciton lifetime, found from the measurements, is 800 – 1200 ps, which complies with the respective value for the arrays of the first type [52]. Note that, for the second type, the growth of the top layer allows the cavities to be formed and the electrical contacts to be applied, which makes it especially suitable for the implementation of nano-antennas.

Lastly, it is relevant to mention that the soliton mechanism of the self-trapping

of the antenna helps to mitigate detrimental effects of imperfections of the underlying QD lattice, as discrete solitons are well known to be robust against deformations of the lattice [6]. Moreover, the fact that the phase structure of topologically organized solitons, such as discrete vortices [51], is stable in imperfect lattices, also indicates that the so constructed nano-antennas tend to stabilize themselves against dephasing.

It is relevant to note that the self-organized lattice built of semiconductor QDs not a unique structure allowing the implementation of soliton-based nano-antennas, and the RO is not a unique enabling mechanism for this. Another promising way for achieving this purpose is suggested by theoretical analysis of discrete dissipative plasmon solitons in an array of graphene QDs [55]. The single QD in such an array represents a doped graphene nanodisk placed on top of the plane background. The single-dot excitation represents a confined surface plasmon with the resonant frequency in the THz or infrared range. The QDs in the array are coupled by long-range dipole-dipole interactions. As it was demonstrated in [55], the soliton formation and its stability take place under the control of an incident driving electromagnetic wave via the Kerr optical nonlinearity. In spite of the different physical origins, both the surface plasmon solitons predicted in [55] and Rabi solitons considered above exhibit strongly confined one- or two-peak areas of electrical polarization. Such peaks may be symmetric or asymmetric, while the spatial structure of the confinement area is tunable via the incidence angle of the oblique driving field. Thus, the above-mentioned graphene QD-array makes it possible to design an electrically controlled nano-antenna for THz and infrared frequency ranges. The radiation pattern (or array factor) for this antenna is given by Eq. (38) with necessary modifications (the slowly varying amplitudes of orthogonally directed dipole moments can be found as a solutions of the nonlinear coupled equations derived in [55]). The qualitative shape of such a radiation pattern is similar to that of the Rabi-soliton-based nano-antenna proposed above.

5. Conclusions

The objective of this work is to introduce the concept of the tunable nano-antenna array based on the discrete-soliton patterns formed in the 2D nonlinear lattices of semiconductor QDs (quantum dots). These lattices can be realized as square-shaped arrays of identical two-level quantum oscillators (the self-organized semiconductor QDs), coupled to nearest neighbors by the electron-hope tunneling and interacting with the external electromagnetic field. The local-field corrections, which account for the difference between the field inside the QD and the external field, induce the nonlinearity of the electron-hole motion inside each QD.

The main conclusions of our study are summarized as follows.

(i) The model of RO (Rabi oscillations) in the 2D QD lattice has been derived, taking the inter-dot tunnelling and local-field correction into account. The model is based on a set of linearly and nonlinearity coupled DNLS equations for probability amplitudes of the ground and first excited states of two-level oscillators (QDs).

Two different driving electromagnetic fields were considered, *viz.*, the plane-wave and cylindrical ones. In the former case, the coupling coefficients are complex, with absolute values independent of the QD position, and phases linearly increasing across the QD array in both directions. For the cylindrical-wave drive, the absolute values of the coupling coefficients depend on the distance between the given QD and the source of the driving field. The corresponding phases depend nonlinearly on the distance.

(ii) Stable discrete-soliton complexes are found. They are built of onsite fundamental single-peaked solitons, taken in both components, or discrete vortex solitons of certain types.

(iii) The emission properties of stable solitary modes have been characterized by angular radiation patterns. These patterns strongly depend on the type of the discrete localized mode.

(iv) The concept of self-assembling nano-antennas, based on the stable discrete-soliton complexes in the nonlinear lattices, is introduced. The necessary type of the localized mode may be selected by the initial conditions, which, in turn, can be controlled by the external optical field (to be supplied in the form of a strong laser pulse). As a consequence, a finite number of predefined radiation patterns can be provided by a given antenna. This way of the operational control of nano-antennas has no analogs in previously developed antenna schemes. The stability of the self-trapped nano-antennas against structural imperfections and intrinsic dephasing has been considered. Thus, the system proposed here can be related to switched-beam systems used in macroscopic antennas [28], which is a promising setting for applications to nanoelectronics and nanooptics.

(v) The concept of soliton-excited nano-antennas may be carried over to the surface-plasmon mechanism of the soliton formation in the array of graphene QDs with the Kerr nonlinearity predicted in [55]. This type of the nano-antennas is promising for applications in the THz and infrared frequency ranges.

Acknowledgements

G.G., A.M., and Lj.H. acknowledge support from the Ministry of Education and Science of Serbia (Project III45010). G.S. acknowledges support from the EU FP7 projects FP7 People 2009 IRSES 247007 CACOMEL and FP7 People 2013 IRSES 612285 CANTOR.

References

- [1] Lederer F, Stegeman G I, Christodoulides D N, Assanto G, Segev M and Silberberg Y 2008 *Phys. Rep.* **463** 1
- [2] Trombettoni A and Smerzi A 2001 *Phys. Rev. Lett.* **86** 2353; Abdullaev F Kh, Baizakov B B, Darmanyan S A, Konotop V V and Salerno M 2001 *Phys. Rev. A* **64** 043606; Alfimov G L, Kevrekidis P G, Konotop V V, and Salerno M 2002 *Phys. Rev. E* **66** 046608; Carretero-González R and Promislow K 2002 *Phys. Rev. A* **66** 033610; Efremidis N K and Christodoulides D N 2003 *ibid.* **67** 063608; Jin G-R, Kim C-K, Nahm K 2005 *ibid.* **72** 045601; Maluckov A, Hadžievski Lj, Malomed B A and Salasnich L 2008 *ibid.* **78** 013616

- [3] Fisher M P A, Grinstein G and Fisher D S 1989 *Phys. Rev. B* **40** 546; Greiner M, Mandel O, Esslinger T, Hansch T and Bloch I 2001 *Nature* **415** 39
- [4] Giamarchi T 2004 *Quantum Physics in One Dimension* (Oxford University Press, Oxford); Bloch I, Dalibard J and Zwerger W 2008 *Rev. Mod. Phys.* **80** 885; Cazalilla M A, Citro R, Giamarchi T, Orignac E and Rigol M 2011 *ibid.* **83** 1405
- [5] Lewenstein M, Sanpera A and Ahufinger V 2012 *Ultracold Atoms in Optical Lattices: Simulating Quantum Many-Body Systems* (Oxford University Press, Oxford)
- [6] Kevrekidis P G 2009 *The Discrete Nonlinear Schrödinger Equation: Mathematical Analysis, Numerical Computations, and Physical Perspectives* (Springer, Berlin)
- [7] Deconinck B, Kevrekidis P G, Nistazakis H E and Frantzeskakis D J 2004 *Phys. Rev. A* **70** 063605
- [8] Ballagh R J, Burnett K and Scott T F 1997 *Phys. Rev. Lett.* **78** 1607
- [9] Ohberg P and Stenholm S 1999 *Phys. Rev. A* **59** 3890
- [10] Williams J, Walser R, Cooper J, Cornell E and Holland M 1999 *Phys. Rev. A* **59** R31
- [11] Herring G, Kevrekidis P G, Malomed B A, Carretero-González R and Frantzeskakis D J 2007 *Phys. Rev. E* **76** 066606
- [12] Engheta N, Salandrino A and Alù A 2005 *Phys. Rev. Lett.* **95** 095504
- [13] *Quantum Dot Lasers* 1998 (edited by M. G. D. Bimberg and N. N. Ledentsov, Wiley, Chichester, England)
- [14] Novotny L and Hecht B 2006 *Principles of Nano-Optics* (Cambridge University Press, New-York)
- [15] Scully M O and Zubairy M S 2001 *Quantum Optics* (Cambridge University Press, Cambridge, England)
- [16] Xie Q-T, Cui S, Cao J-P, Amico L and Fan H 2014 *Phys. Rev. X* **4** 021046
- [17] Slepyan G Ya, Maksimenko S A, Hoffmann A and Bimberg D 2002 *Phys. Rev. A* **66** 063804
- [18] Slepyan G Ya and Maksimenko S A 2008 *New J. Phys.* **10** 023032
- [19] Slepyan G Ya, Magyarov A, Maksimenko S A, Hoffmann A and Bimberg D 2004 *Phys. Rev. B* **70** 045320
- [20] Slepyan G Ya, Magyarov A, Maksimenko S A and Hoffmann A 2007 *Phys. Rev. B* **76** 195328
- [21] Kibis O V, Slepyan G Ya, Maksimenko S A and Hoffmann A 2009 *Phys. Rev. Lett.* **102** 023601
- [22] Slepyan G Y, Yerchak Y, Maksimenko S A and Hoffmann A 2009 *Phys. Lett. A* **373** 1374
- [23] Slepyan G Y, Yerchak Y D, Hoffmann A and Bass F G 2010 *Phys. Rev. B* **81** 085115
- [24] Slepyan G Y, Yerchak Y D, Maksimenko S A, Hoffmann A and Bass F G 2012 *Phys. Rev. B* **85** 245134
- [25] Mitsumori Y, Hasegawa A, Sasaki M, Maruki H and Minami F 2005 *Phys. Rev. B* **71** 233305
- [26] Asakura K, Mitsumori Y, Kosaka H, Edamatsu K, Akahane K, Yamamoto N, Sasaki M and Ohtani N 2013 *Phys. Rev. B* **87** 241301(R)
- [27] Gligorić G, Maluckov A, Hadžievski Lj, Slepyan G Ya and Malomed B A 2013 *Phys. Rev. B* **88** 155329
- [28] Balanis C A 1997 *Antenna Theory: Analysis and Design* (New York: Wiley)
- [29] Biagioni P, Huang Y-S and Hecht B 2012 *Rep. Prog. Phys.* **75** 024402
- [30] Novotny L and van Hulst N 2011 *Nature Photonics* **5** 83
- [31] Engheta N 2007 *Science* **317** 1698
- [32] Hanson G W 2005 *IEEE Trans. Antennas Propag.* **53** 3426
- [33] Burke P J, Li S and Yu Z 2006 *IEEE Trans. Nanotechnol.* **5** 314
- [34] Slepyan G Ya, Shuba M V, Maksimenko S A and Lakhtakia A 2006 *Phys. Rev. B* **73** 195416
- [35] Ren L, Zhang Q, Pint C L, Wójcik A K, Bunney M, Arikawa Jr T, Kawayama I, Tonouchi M, Hauge R H, Belyanin A A and Kono J 2013 *Phys. Rev. B* **87** 161401(R)
- [36] Novotny L 2007 *Phys. Rev. Lett.* **98** 266802
- [37] Alù A and Engheta N 2008 *Phys. Rev. Lett.* **101** 043901
- [38] Jornet J M and Akyildiz I F 2013 *IEEE J. Selected Areas in Communications/ Supplement* **p.2** **31** 685
- [39] Slepyan Gr Y and Boag A. 2013 *Phys. Rev. Lett.* **111** 023602

- [40] Landau L D and Lifshitz E M 1980 *Statistical Physics* (Pergamon, New York).
- [41] Mokhlespour S, Haverkort J E M, Slepyan G, Maksimenko S and Hoffmann A 2012 *Phys. Rev. B* **86** 245322
- [42] Zheng Z, Zhao C, Lu S, Chen Yu, Li Y, Zhang H and Wen S 2012 *Optics Express* **20** 23201
- [43] Zhang H, Virally S, Bao Q, Ping L K, Massar S, Godbout N and Kockaert P 2012 *Opt. Lett.* **37** 1856
- [44] Asakura K, Mitsumori Y, Kosaka H, Edamatsu K, Akahane K, Yamamoto N, Sasaki M, and Ohtani N 2013 *Phys. Rev. B* **87**, 241301(R)
- [45] Citrin D S 1993 *Phys. Rev. B* **48** 2535
- [46] Slepyan G Ya, Maksimenko S A, Lakhtakia A, Yevtushenko O and Gusakov A V 1999 *Phys. Rev. B* **60** 17136
- [47] Gligorić G, Maluckov A, Stepić M, Hadzievski Lj and Malomed B A 2010 *Phys. Rev. A* **81** 013633
- [48] Gligorić G, Maluckov A, Stepić M, Hadzievski Lj and Malomed B A 2010 *J. Phys. B: At. Mol. Opt. Phys.* **43** 055303
- [49] Öster M and Johansson M 2006 *Phys. Rev. E* **73** 066608
- [50] Kevrekidis P G, Rasmussen K O and Bishop A R 2000 *Phys. Rev. E* **61** 2006
- [51] Malomed B A and Kevrekidis P G 2001 *Phys. Rev. E* **64** 026601
- [52] Miyazaki J and Kinoshita S 2012 *Phys. Rev. B* **86** 035303
- [53] Ding C R, Wang H Z and Xu B 2005 *Phys. Rev. B* **71** 085304
- [54] Fox M 2012 *Quantum Optics: An Introduction* (Oxford Master Series: Oxford University Press)
- [55] Smirnova D A, Noskov R E, Smirnov L A and Kivshar Y S 2015 *Phys. Rev. B* **91** 075409